Detection of the Water-Binding Sites of the Oxygen-Evolving Complex of Photosystem II Using W-Band ^{17}O Electron–Electron Double Resonance-Detected NMR Spectroscopy

Leonid Rapatskiy,[†] Nicholas Cox,*[,†] Anton Savitsky,[†] William M. Ames,[†] Julia Sander,[‡] Marc. M. Nowaczyk,[‡] Matthias Rögner,[‡] Alain Boussac,[§] Frank Neese,[†] Johannes Messinger,[‖] and Wolfgang Lubitz*[,†]

[†]Max-Planck-Institut für Chemische Energiekonversion, Stiftstrasse 34-36, D-45470 Mülheim an der Ruhr, Germany
[‡]Plant Biochemistry, Ruhr University Bochum, Universitätsstrasse 150, D-44780 Bochum, Germany
[§]iBiTec-S, URA UMR 8221, CEA Saclay, 91191 Gif-sur-Yvette, France
[‖]Department of Chemistry, Chemical Biological Centre (KBC), Umeå University, S-90187 Umeå, Sweden

S *Supporting Information*

ABSTRACT: Water binding to the Mn_4O_5Ca cluster of the oxygen-evolving complex (OEC) of Photosystem II (PSII) poised in the S_2 state was studied via $H_2^{17}O$- and ^2H_2O-labeling and high-field electron paramagnetic resonance (EPR) spectroscopy. Hyperfine couplings of coordinating ^{17}O ($I = ^5/_2$) nuclei were detected using W-band (94 GHz) electron–electron double resonance (ELDOR) detected NMR and Davies/Mims electron–nuclear double resonance (ENDOR) techniques. Universal ^{15}N ($I = ^1/_2$) labeling was employed to clearly discriminate the ^{17}O hyperfine couplings that overlap

with ^{14}N ($I = 1$) signals from the D1-His332 ligand of the OEC (Stich et al. *Biochemistry* **2011**, *50* (34), 7390−7404). Three classes of ^{17}O nuclei were identified: (i) one μ-oxo bridge; (ii) a terminal Mn−OH/OH$_2$ ligand; and (iii) Mn/Ca−H$_2$O ligand(s). These assignments are based on ^{17}O model complex data, on comparison to the recent 1.9 Å resolution PSII crystal structure (Umena et al. *Nature* **2011**, *473*, 55−60), on NH$_3$ perturbation of the ^{17}O signal envelope and density functional theory calculations. The relative orientation of the putative ^{17}O μ-oxo bridge hyperfine tensor to the $^{14}N(^{15}N)$ hyperfine tensor of the D1-His332 ligand suggests that the exchangeable μ-oxo bridge links the outer Mn to the Mn_3O_3Ca open-cuboidal unit (O4 and O5 in the Umena et al. structure). Comparison to literature data favors the Ca-linked O5 oxygen over the alternative assignment to O4. All ^{17}O signals were seen even after very short (≤15 s) incubations in $H_2^{17}O$ suggesting that all exchange sites identified could represent bound substrate in the S_1 state including the μ-oxo bridge. $^1H/^2H$ ($I = ^1/_2$, 1) ENDOR data performed at Q- (34 GHz) and W-bands complement the above findings. The relatively small $^1H/^2H$ couplings observed require that all the μ-oxo bridges of the Mn_4O_5Ca cluster are deprotonated in the S_2 state. Together, these results further limit the possible substrate water-binding sites and modes within the OEC. This information restricts the number of possible reaction pathways for O−O bond formation, supporting an oxo/oxyl coupling mechanism in S_4.
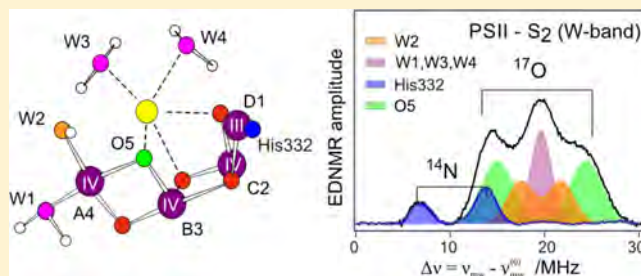
1. INTRODUCTION

In oxygenic photosynthesis, light-driven water splitting is catalyzed by the oxygen-evolving complex (OEC) of Photosystem II (PSII). The OEC consists of an inorganic Mn_4O_5Ca cluster and its surrounding protein matrix.[1−8] The functionally important protein matrix includes the redox-active tyrosine residue Y_Z (D$_1$-Y_{161}). Y_Z couples electron transfer from the Mn_4O_5Ca cluster to $P_{680}^{•+}$ and is involved in proton transfer reactions.[9] $P_{680}/P_{680}^{•+}$ and Pheo/Pheo$^{•−}$ form the primary component of the photoactive reaction center of PSII, which energetically drives water splitting by four sequential light-induced charge separations, for reviews see refs 5−8,10,11. During water splitting, the Mn_4O_5Ca cluster steps through a reaction cycle comprising five distinct redox intermediates.

These are known as the S_n states, where the subscript indicates the number of stored oxidizing equivalents ($n = 0−4$).[12] Once formed, the $S_3Y_Z^{•}$ state rapidly decays to the S_0 state with the concomitant release of molecular triplet oxygen and the rebinding of at least one substrate water molecule.[10] A S_4 state, which is different from the $S_3Y_Z^{•}$ state, has not yet been spectroscopically identified. The S_1 state is thermodynamically stable, and samples left in the dark for minutes to hours equilibrate primarily in this state. The next state S_2 can be formed via either flash illumination at room temperature or via low temperature illumination at 200 K, as it requires no large

protein conformation change. This structural invariance is unique to the $S_1 \rightarrow S_2$ transition.

The structure of PSII, including the OEC was recently determined at a resolution of 1.9 Å by Umena et al.[1] The position of all four Mn ions of the OEC and the network of five bridging μ-oxo ligands connecting the metal ions were resolved. The proposed structure bears similarities to earlier literature models,[2] including those derived from (polarized) extended X-ray absorption fine structure (EXAFS) measurements[4,13] and to the computational models of Kusunoki,[14] Siegbahn,[6] and Dau.[7,15] The Umena model has a distorted chairlike structure where the base is formed by a μ-oxo-bridged cuboidal Mn_3O_4Ca unit (Figure 1A). The fourth "outer" manganese,
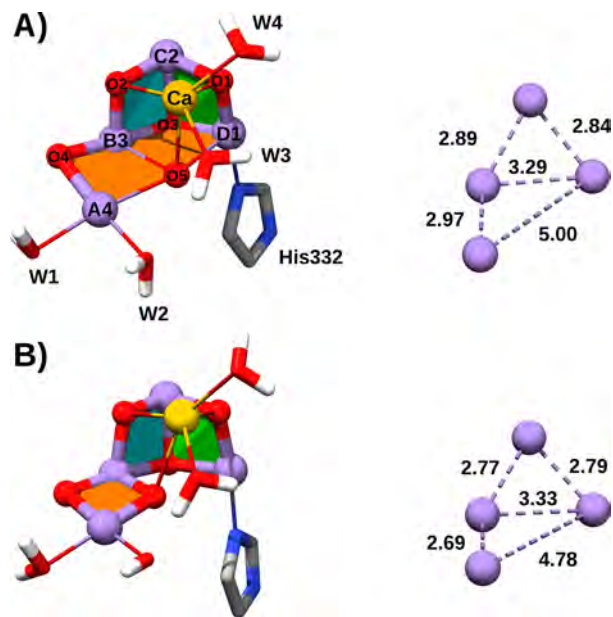
Figure 1. Topography of the Mn_4O_5Ca cluster of the OEC. (A) The crystal structure model of Umena et al.[1] (B) A recent representative computational model of Ames et al.[19] The right-hand side structures show the five Mn−Mn distances of the cluster. Atom numbering combines the polarized EXAFS[4] nomenclature (Mn_A, Mn_B, etc) with that of Umena et al.[1] (Mn_1, Mn_2, etc). Atom coloring is as follows: Mn, purple; Ca, yellow; O, red; N, blue; H, white. W1−W4 stand for water molecules/hydroxo groups identified in the crystal structure.[1] The three Mn−(μO)$_2$−Mn planes of the μ-oxo bridge subunits of the OEC are colored orange, green, and turquoise.

Mn_{A4} (this nomenclature combines the numbering based on polarized EXAFS[4] models with that of Umena et al.[1]), is attached to this core structure via a μ-oxo-bridged ligation (O4) and by one hydroxo bridge (O5) to the central manganese, Mn_{B3}. Compared to the experimental EXAFS data, the Mn−Mn, Mn−Ca, and Mn−O/N distances determined from the crystal structure are all elongated, suggesting that the cluster underwent some degree of radiation-induced reduction during data collection and thus may represent a "super-reduced" S state (S_{-1}, S_{-2}, S_{-3})[16] that can also be generated via chemical reduction (NH_2OH, NH_2NH_2) of the cluster.[17] Nevertheless, the general pattern of three short and one long Mn−Mn distances and four Mn−Ca distances as observed in EXAFS measurements is preserved.[4,13,18]

In the Umena structure, the central O5 has unusually long bonds to three Mn ions and to the Ca ion. It was suggested that it represents a hydroxo group or a water molecule and is

potentially one of the substrate "waters" (the term substrate water does not distinguish between the three possible protonation states, water/hydroxo/oxo). In contrast, in polarized EXAFS models and in most computational models, O5 is a μ-oxo bridge between Mn_{A4} and Mn_{B3} in the S_1 and S_2 states, rendering this unit bis-μ-oxo bridged, and Mn_{D1} as five coordinate.[6,19,20] One such computational model, proposed in the recent density functional theory (DFT) study performed by our laboratory,[19] is shown in Figure 1B. A bis-μ-oxo bridged linkage between Mn_{A4} and Mn_{B3} was found to be energetically favorable and engendered Mn−Mn distances and magnetic properties consistent with EXAFS and electron paramagnetic resonance/electron−nuclear double resonance (EPR/ENDOR) data.

To elucidate the mechanism of water oxidation to molecular oxygen, it is crucial to identify which of the water-derived ligands represent the two substrate molecules. Time-resolved $H_2^{16}O/H_2^{18}O$ exchange membrane inlet mass spectrometry experiments have shown that at least one substrate water (the slowly exchanging, W_s) is bound in all S states and that its exchange kinetics are significantly affected by replacement of the Ca ion with Sr.[21,22] Water bound at this substrate site exchanges with the bulk water on a seconds time scale, with the slowest exchange rate observed in the S_1 state ($k_s \sim 0.02−0.066$ s^{-1}).[10] The second, faster exchanging substrate water (W_f) has been shown to bind in the S_3 state and possibly already in the S_2 state.[22−24] W_f exchanges much faster than W_s, on a subsecond time scale ($k_s = 40−120$ s^{-1}). FTIR measurements provide independent information about the binding site and mode of water molecules in the various S_n states.[25,26] These data indicate that one water molecule, possibly W_f, binds during the $S_2 \rightarrow S_3$ transition. The binding of W_f in this transition is a key feature in the oxo/oxyl coupling mechanism of water oxidation proposed by Siegbahn based on DFT calculations.[6,27]

EPR spectroscopy is a powerful tool for determining the identity ($H_2O/^-OH/O^{2-}$) and location of water-derived species bound in the vicinity of the Mn_4O_5Ca cluster. In the paramagnetic S_2 and S_0 states, water-exchangeable protons can be identified via the disappearance of signals originating from the hyperfine couplings of ^1H nuclei ($I = ^1/_2$) to the net electronic spin ($S_T = ^1/_2$) of the Mn_4O_5Ca cluster after $^1H_2O/^2H_2O$ exchange. Kawamori et al.[28] were the first to report ^1H couplings to the OEC obtained from spinach, poised in the S_2 state using X-band continuous wave (cw)-ENDOR. The measured ^1H envelope extended out from the ^1H-nuclear Larmor frequency by ±2 MHz and disappeared after resuspension of the PSII in buffer made in ^2H_2O. These results were interpreted as evidence for water molecule(s) directly coordinating to one or more Mn ions (^1H at a distance of 2−3 Å from a Mn). The first attempt at a quantitative fitting of the ^1H envelope was performed in the pulse ^1H-ENDOR and ^2H-electron spin echo envelope modulation (ESEEM) studies of Britt et al.[29,30] Here, a four shell model (inclusive of ambient water) was developed with electron−nuclear dipolar hyperfine couplings (A_{dip}) similar to those seen in earlier studies.[28,31] As before, these results were interpreted as evidence for a direct Mn−water interaction, fixing the number of protonated coordinating water molecules to two. Similar hyperfine couplings were estimated for the S_0 state, and approximately the same number of Mn−proton interactions were inferred.[30] A subsequent X-band ^2H-ESEEM study by Ahrling et al.[32] reached a similar conclusion albeit with an increase of the

A_{dip} of the largest hyperfine tensor that was also seen in the recent X-band HYSCORE studies of Martínez et al.[33]

A more direct probe for water-derived ligands is via the direct detection of oxygen using ^{17}O labeling. One particular advantage is that the fully deprotonated substrate state, for example, the incorporation of a water into a Mn-μ-oxo bridge, can be identified. Only a small number of publications describing ^{17}O couplings of metallocofactors and related model complexes have been published to date (see refs 34−38 for examples and the Supporting Information, S2). This is due to a combination of factors, including the low natural abundance (0.038%) of ^{17}O and as a consequence the high costs for enrichment, the large nuclear spin ($I = ^5/_2$) and small nuclear g-factor (−0.7575) of ^{17}O, and significant quadrupole coupling value ($e^2Qq/h \sim 6$ MHz).[39] The first ^{17}O labeling X-band cw-EPR study reported in PSII attempted to resolve line broadening of the individual lines of the S_2 multiline spectrum due to the coupling of the Mn ions to an ^{17}O nucleus.[40] This was followed by the X-band ESEEM study of the Nugent/Evans laboratory.[41,42] The authors clearly identified only a matrix ^{17}O signal but also speculated that a second species may be observed that gives rise to a larger hyperfine coupling of about 5 MHz. However, owing to the large number of overlapping background ^{14}N signals (see below), this latter assignment was considered tentative. The next ^{17}O study used X-band HYSCORE to characterize substrate binding.[43] Two sharp peaks were observed centered about the Larmor frequency of ^{17}O and were assigned to the coupling of a ^{17}O nucleus to the Mn complex. It has been recently demonstrated that this assignment is incorrect[44] and that these signals should be attributed to couplings of ^{14}N to the cytochrome b559.[45] Finally, a broad Q-band ^{17}O-ENDOR signal at about 15 MHz has very recently been observed in higher plant PSII.[46] This signal was assigned to a μ-oxo bridge based on its similarity to a broad, structureless signal seen for the labeled $Mn^{III}−(\mu O)_2−Mn^{IV}$ BIPY complex.[47] The μ-oxo bridge species observed was considered to exchange with bulk water on a time scale of the order of $10^4−10^5$ s and as a consequence represents a slowly exchanging structural site as opposed to a substrate of the catalyst.[48] Similar slow rates of exchange for μ-oxo bridges have been observed in synthetic Mn model systems.[49]

In this work, we present an EPR investigation of water binding to the Mn_4O_5Ca cluster via measurement of ^{17}O-hyperfine couplings. In order to obtain complete ^{17}O hyperfine-patterns and discriminate these from those of ^{14}N nuclei, the EPR experiments were performed at W-band using the electron−electron double resonance (ELDOR)-detected NMR technique (EDNMR).[50] While this technique was reported almost 20 years ago, it has only recently been used for the study of low γ nuclei,[51,52] such as ^{17}O.[53,54] As a consequence, model systems were examined first to better gauge the advantages and limitations of this technique. The enhanced nuclear frequency resolution at high magnetic fields of about 3.4 T (W-band) in conjunction with the superior sensitivity of EDNMR as compared to ENDOR, allows clear assignments of water-derived ligands of the Mn_4O_5Ca cluster, which were resolved in the recent 1.9 Å structure of PSII.[1] In addition, time-resolved water-exchange experiments also provide direct comparison to the kinetics of substrate binding as determined earlier by time-resolved membrane inlet mass spectrometry experiments.[22,23]

2. MATERIALS AND METHODS

2.1. PSII Sample Preparation. PSII core complex preparations from WT* *Thermosynechococcus elongatus*[55] were isolated as described earlier.[56−58] Universal ^{15}N labeling of the PSII preparation was achieved by growing the cyanobacteria in modified BG11 media that contained $^{15}NH_4Cl$ as the sole nitrogen source.[59] Samples were stored at −80 °C until use. Dark-adapted samples were placed in Q-band (1.6 mm I.D.) and W-band (0.6 mm I.D.) quartz tubes. The sample concentration was 3.0−4.0 mg of Chl/mL for both Q- and W-band samples. The S_2 state was generated by short, white light illumination (5 s) with a tungsten lamp at 200 K using a dry ice/ethanol bath.

Resuspension of PSII samples in labeled $H_2^{17}O$ (90%) and ^2H_2O (99%) buffer was achieved as follows. The $H_2^{17}O$ and ^2H_2O buffers were composed of the following: 20 mM 2-(N-morpholino)-ethanesulfonic acid (MES); 10 mM $MgCl_2$; 10 mM NaCl; 0.03% dodecyl maltoside (DDM); and 50 mM mannitol. For the $H_2^{17}O$ buffer, the buffer ingredients were first dissolved at 10-fold higher concentrations in unlabeled water. This stock solution was then added to clean $H_2^{17}O$ (1:10 v/v) to make the labeled buffer. As a final step, the buffers were poised at a pH of 6.5 (MES/NaOH) and pD 6.5 (MES/NaOD). The PSII sample was diluted by 50% in the isotopically labeled buffer and reconcentrated to the initial concentration using Millipore microcentrifuge filters (Amicon Ultra-0.5 mL, 100 kDa). This isotope enrichment procedure was repeated three times. The final enrichment of ^{17}O was estimated to be greater than 70%.

"Rapid dilution" experiments were also performed for PSII W-band samples. In these experiments, the PSII sample was not resuspended into the labeled $H_2^{17}O$ buffer but instead simply diluted by the $H_2^{17}O$ (90%). In this way, the total exchange time could be reduced to the seconds time scale. In these experiments, $H_2^{17}O$ water (1−1.5 μL) was placed at the bottom of the W-band sample tube. The unlabeled PSII sample (1−1.5 μL) was then added to the tube 5−10 mm above the level of the water. Capillary action prevented the mixing of the two components. The W-band tube was then placed in a benchtop centrifuge (Fischer Scientific, model 3722 L) and spun for approximately 2 s. The sample was then rapidly frozen in liquid nitrogen. The entire procedure took less than 15 s from the start of the spin cycle to the freezing of the sample. High isotope enriched $H_2^{17}O$ (90%) was used to maximize sample labeling, which theoretically cannot exceed 45% in these samples.

2.2. Q-Band EPR Measurements. Q-band pulse EPR and ^1H- and ^2H-ENDOR measurements were performed at 4.8 K using a Bruker ELEXSYS E580 Q-band pulse EPR spectrometer equipped with a home-buildt TE_{011} microwave cavity[60] and an Oxford-CF935 liquid helium cryostat. Electron spin echo-detected (ESE) field-swept spectra were measured using the following pulse sequence: $t_p−\tau−2t_p−\tau−$echo. The length of the $\pi/2$ microwave pulse was generally set to $t_p = 12$ ns. The interpulse distance was varied in the range $\tau = 200−500$ ns. ^1H-ENDOR spectra were acquired using the Davies-type pulse sequence: $t_{inv}−t_{RF}−T−t_p−\tau−2t_p−\tau−$echo using an inversion microwave pulse of length $t_{inv} = 128$ ns and a radio frequency (RF) π pulse of length $t_{RF} = 20$ μs. The length of the $\pi/2$ microwave pulse in the detection sequence was generally set to $t_p = 64$ ns and the interpulse delays to $T = 1.5$ μs and $\tau = 468$ ns. The RF frequency was swept 20 MHz around the ^1H-Larmor frequency of about 53 MHz (1.2 T) in 50 kHz steps. ^2H-ENDOR spectra were collected using the Mims-type pulse sequence: $t_p−\tau−t_p−t_{RF}−T−t_p−\tau−$echo, with $t_p = 16$ ns, $t_{RF}= 40$ μs, $\tau = 300−500$ ns, and $T = 2$ μs. The RF frequency was swept 2 MHz around the ^2H-Larmor frequency of about 8 MHz (1.2 T) in 6.67 kHz steps.

2.3. W-Band EPR Measurements. High-field EPR experiments were performed at 4.8 K using a W-band EPR spectrometer (Bruker ELEXSYS E680) operating at about 94 GHz. All experiments were carried out using a home-built ENDOR microwave cavity, which contained a solenoid of Teflon coated silver wire integrated into a commercial W-band ENDOR probehead (Bruker). The RF coil contains 20 turns for optimized RF performance at low RF frequencies (<100 MHz, optimum performance at 20 MHz). To ensure
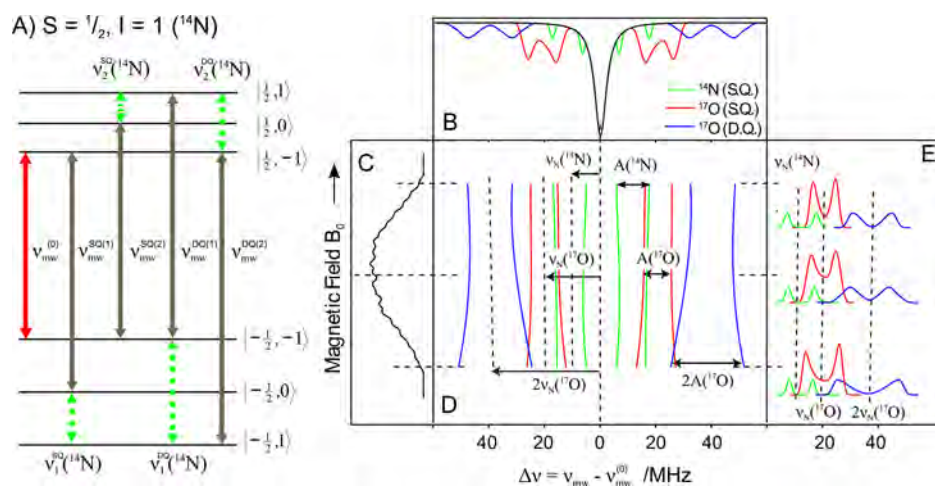
Figure 2. Simulated W-band EDNMR spectra of a mixed-valence Mn-dimer complex ($S = 1/2$) containing weakly anisotropically coupled low-γ nuclei (^{17}O, ^{14}N). (A) The energy levels of an $S = 1/2$, $I = 1$ (^{14}N) spin manifold showing the allowed (EPR, $\nu_{mw}^{(0)}$, red), forbidden (ELDOR, $\nu_{mw}^{SQ(1)}$, $\nu_{mw}^{DQ(1)}$, etc, gray) and corresponding NMR (ν_1^{SQ} (^{14}N), ν_1^{DQ} (^{14}N), etc, green) transitions of the manifold. S.Q. and D.Q. refer to single and double quantum transitions, respectively. (B) The EDNMR spectrum measured at the center of the multiline spectrum. (C) The EPR multiline spectrum of the complex in field sweep mode. (D) The two-dimensional (2D) EDNMR surface representation of B. (E) The baseline-corrected EDNMR spectrum at three selected field positions within C: the center field and the low and high field edge. Only half the EDNMR spectrum is shown and inverted for clarity of presentation. Simulation parameters used for the EPR line shape are approximately those fitted for the mixed valence Mn^{III}Mn^{IV} BIPY complex[63], see Table 1.

broadband microwave excitation and to minimize the distortions caused by high-power RF excitation, the loaded quality factor, Q_L, was lowered to 700 to obtain a microwave frequency bandwidth of 130 MHz.

Electron spin echo-detected (ESE) field-swept spectra were measured using the following pulse sequence: $t_p-\tau-2t_p-\tau-$echo with $t_p = 24$ ns and $\tau = 200-500$ ns. ^{17}O–Davies ENDOR spectra were collected using the following pulse sequence: $t_{inv}-t_{RF}-T-t_p-\tau-2t_p-\tau-$echo with $t_{inv} = 128$ ns, $t_p = 24$ ns, $t_{RF} = 15$ μs, $T = 1$ μs, and $\tau = 348$ ns. ^{17}O-Mims ENDOR spectra were collected using the following pulse sequence: $t_p-\tau-t_p-t_{RF}-T-t_p-\tau-$echo, with $t_p = 24$ ns, $t_{RF} = 15$ μs, $\tau = 300-500$ ns, and $T = 1$ μs. In both ENDOR experiments, the RF frequency was swept 6.4 MHz around the ^{17}O-Larmor frequency of about 19.7 MHz (3.4 T) in 43 kHz steps.

ELDOR-detected NMR (EDNMR) measurements were done using the following pulse sequence: $t_{HTA}-T-t_p-\tau-2t_p-\tau-$echo. The high-turning-angle (HTA) microwave pulse was applied at microwave frequency ν_{mw}. The detection Hahn echo pulse sequence $t_p-\tau-2t_p-\tau-$echo at microwave frequency $\nu_{mw}^{(0)}$, matched to the cavity resonance, was set 6 μs after the HTA pulse to ensure near-complete decay of the electron spin coherencies. The $\pi/2$ pulse length used for detection was $t_p = 100$ ns, and an interpulse separation of $\tau = 500$ ns was generally used. The echo was integrated 600 ns around its maximum. The spectra were acquired via continuously sweeping the HTA frequency ν_{mw} at fixed B_0 in steps of 68.4 kHz. A low-power HTA microwave pulse of $t_{HTA} = 8-14$ μs length and amplitude of $\omega_1 = (4-6) \times 10^6$ rad·s^{-1} was used to minimize the width of the central blind spot (see Section 2.5) to allow resolution of the low frequency ^{14}N(^{15}N) spectral lines. The microwave settings of the EDNMR experiment do not represent the optimal conditions for the resolution of ^{17}O-hyperfine couplings but instead are a compromise that allows simultaneous detection of both ^{14}N and ^{17}O responses from both single and double quantum transitions, minimally perturbed by the central blind spot (see Section 2.5).

2.4. Spectral Simulations. Spectra were simultaneously fit assuming an effective spin $S = 1/2$ ground state (for details see the Supporting Information, S3 and S4). The basis set that describes the ^{17}O/^{14}N–Mn-tetramer spin manifold can be built from the product of the eigenstates of the interacting spins:

$$\left| \frac{1}{2} \, M \, I \, m \right\rangle \tag{1}$$

Here, M refers to the electronic magnetic sublevel, $\pm 1/2$; I takes the value $5/2$ for ^{17}O, 1 for ^{14}N, and $1/2$ for ^{15}N; m takes the values $-I, 1-I, ..., I-1, I$.

The spin Hamiltonian that describes the single nucleus–electron spin manifold is as follows:

$$\hat{H} = \beta_e \vec{B}_0 \cdot \hat{G} \cdot \vec{S} + g_o \beta_n \vec{B} \cdot \hat{I} + \vec{S} \cdot \hat{A} \cdot \vec{I} \tag{Eq. 2}$$

It contains (i) the Zeeman term for the total electronic spin; (ii) the Zeeman term for the ^{17}O/^{14}N/^{15}N nucleus; and (iii) the hyperfine term for the ^{17}O/^{14}N/^{15}N nucleus. This Hamiltonian was used to simulate all spectra. The electron Zeeman term was treated exactly. The nuclear Zeeman and hyperfine terms were treated using second order perturbation theory. The nuclear quadrupole coupling was not explicitly considered. Spectral simulations were performed numerically using Scilab-4.4.1, an open source vector-based linear algebra package (www.scilab.org) and the EasySpin package[61] in MATLAB. Spin Hamiltonian parameters were optimized using a least-squares minimization routine.

2.5. EPR Techniques for Measuring Nuclear Transition Frequencies. There are several pulsed EPR techniques that are capable of probing nuclear transition frequencies of paramagnetic compounds: ESEEM-based techniques, ENDOR, and ELDOR-detected NMR.[62] ESEEM is a so-called *coherence-transfer* technique in which the nuclear frequencies are obtained from the analysis of the time-dependent electron spin–echo modulation caused by the oscillation between allowed and forbidden electron coherences or by the evolution of nuclear coherencies. ESEEM is particularly sensitive for the detection of nuclear frequencies in the low-frequency range (below 20 MHz), relatively narrow NMR lines, and moderate spin relaxation rates. In the case of broad NMR lines, the ESEEM techniques suffer from the long dead times of the EPR spectrometer and the finite bandwidth of microwave excitation. In a *polarization-transfer* pulsed EPR experiment, such as ENDOR and EDNMR, the nuclear frequencies are detected by manipulating the polarizations of electron and nuclear levels. The principal difference between ENDOR and EDNMR is the way in which the population of the nuclear levels is changed. In pulse ENDOR, the nuclear polarization is inverted by driving the allowed NMR transition ($\Delta m_S = 0$; $\Delta m_I = \pm 1$, Figure 2A) with a radio frequency (RF) π-pulse. In contrast, in EDNMR, the nuclear transitions of the spin manifold are probed indirectly by using a second high-turning-angle (HTA) microwave pulse, which drives
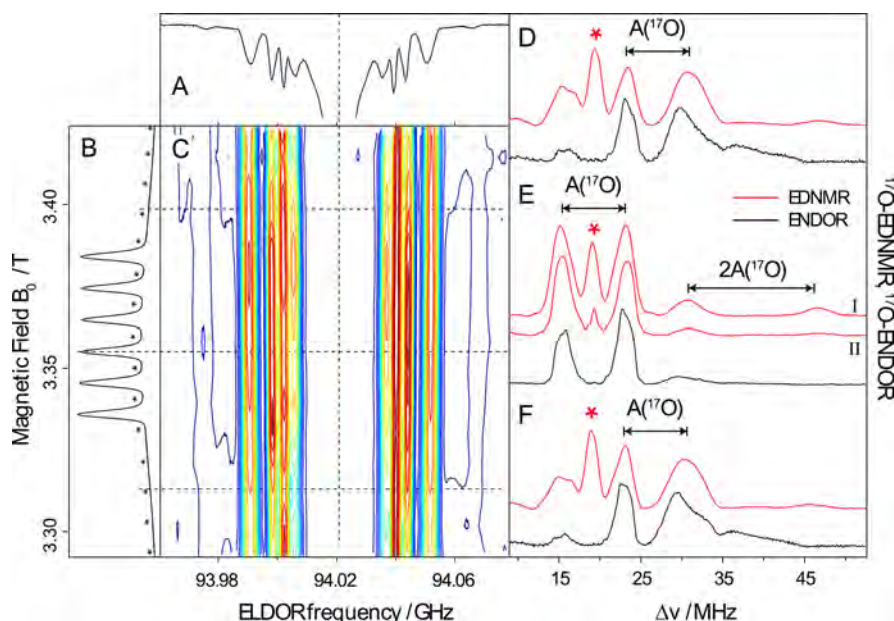
Figure 3. Comparison of W-band ^{17}O Davies ENDOR and EDNMR of $Mn^{II}(H_2{}^{17}O)_6$. (A) the EDNMR spectrum measured at the center field. (B) The EPR multiline spectrum of the complex. (C) 2D EDNMR surface. (D−F) Comparison of the EDNMR signal to the Davies ENDOR signal seen at three field positions, the low field edge 3.320 T (D), the third central line 3.355 T (E), and the high field edge 3.400 T (F). For (C), the EDNMR traces were measured with HTA pulses that varied in amplitude (ω_1) (I) $\omega_1^{HTA} = 1.8 \times 10^6$, vs (II) $\omega_2^{HTA} = 0.8 \times 10^6$ rad·s^{-1}.

forbidden electron transitions, that is, transitions where both the electron and nuclear spin change their projection direction (Figure 2A). The pump pulse is swept around the resonance frequency, $\nu_{mw}^{(0)}$ of the detection Hahn-echo pulse sequence. At microwave frequencies, where the HTA pulse coincides with the forbidden electron transitions ($\Delta m_S = \pm 1$; $\Delta m_I = \pm 1$) of the spin manifold ($\nu_{mw}^{(1)}$, $\nu_{mw}^{(2)}$, Figure 2A), the observed primary echo signal decreases due to population transfer via forbidden transitions. These ν_{mw} dependent signal changes are detected as spectral lines, which correspond to the nuclear transitions of the spin manifold. In addition, the HTA pulse excites the allowed transitions of the spin manifold ($\nu_{mw}^{(0)}$). This results in a decrease of the observed primary echo across the entire swept region. For a rectangular pump pulse, the response profile (central blind spot) is Lorentzian centered at $\nu_{mw}^{(0)}$ with $\Delta\nu_{1/2} = \omega_1^{HTA}/\pi$, where ω_1^{HTA} is the amplitude of the HTA microwave pulse. For an inhomogeneously broadened EPR line, where the EPR line width is larger than that of the nuclear coupling of interest, the nuclear spectral lines appear symmetrically about the central frequency, $\nu_{mw}^{(0)}$.

At high magnetic field (W-band EPR), the nuclear Larmor frequency of many low-γ nuclei (^{2}H, ^{14}N, ^{17}O, etc) is sufficiently large so that the signals from these nuclei can be resolved from the central blind spot, especially for the case in which the hyperfine coupling of the nuclei to the electronic spin is weak, that is, less than twice the Larmor frequency. The W-band EDNMR spectrum of a complex containing both ^{14}N and ^{17}O ligands in the weak-coupling limit is shown as a diagram in Figure 2B. The lines associated with a particular nucleus are centered around the Larmor frequency of the nucleus of interest, split by the hyperfine (and quadrupole) coupling (see the Supporting Information, S7). Importantly, at high magnetic fields, the Larmor frequency of ^{17}O ($\nu_N(^{17}O) = 19.6$ MHz at 3.4 T) is significantly different from that of ^{14}N ($\nu_N(^{14}N) = 10.4$ MHz at 3.4 T), thus allowing both components to be readily resolved. For nuclei that have a nuclear spin greater than $^1/_2$, multiple quantum transitions ($\Delta m_S = \pm 1$, $\Delta m_I = \pm 2$, ...) can be observed. These are centered around multiples of the Larmor frequency split by the same multiple, that is, in the case of double quantum transitions ($\Delta m_S = \pm 1$, $\Delta m_I = \pm 2$), these are now centered about twice the Larmor frequency split by twice the hyperfine coupling (see the Supporting Information, S7).

In the two-dimensional (2D) experiment, an EDNMR spectrum is taken at a series of magnetic field positions across the EPR spectrum

(Figure 2C). A 2D EDNMR surface is shown in Figure 2D. As the nuclear Larmor frequency is linearly field dependent, the mean peak positions of the nuclear lines linearly increases with respect to the central frequency ($\nu_{mw}^{(0)}$) as the magnetic field increases. As a consequence, not only the position but also the rate of change of the peak shift is characteristic of a particular nucleus and as such can be used as a marker for the identity of the nucleus. It is noted that double-quantum transitions must have a field dependence twice that of the corresponding single-quantum transitions.

Compared to ENDOR, high-field EDNMR presents several advantages for the investigation of low-γ nuclei coupled to the electron spin of metalloproteins. EDNMR is more robust against fast electron spin−lattice relaxation, T_1, and spectral diffusion than ENDOR. This robustness is because no preparation of the electron spin system prior to the HTA pulse is required and short HTA pulses can be realized with the available microwave power. This results in high sensitivity and allows one to record 2D-EDNMR spectra with a sufficient signal-to-noise ratio rapidly. Moreover, the recorded EDNMR spectrum is not distorted either by blind spots around the nuclear Larmor frequencies or by a possible frequency dependence of the RF excitation amplitude. These advantages are demonstrated using a simple model system, $Mn^{II}(H_2{}^{17}O)_6$ (Figure 3). The study of Baute and Goldfarb[39] showed that the ^{17}O signals arising from the hyperfine splitting of the ^{17}O nucleus within the $m_s = \pm{}^1/_2$ and $m_s \pm {}^3/_2$ sublevels of the Mn^{II} electron spin manifold could be readily detected at W-band using Davies ENDOR. The corresponding EDNMR of the $Mn^{II}(H_2{}^{17}O)_6$ complex is also shown in Figure 3 (red traces). At the three field positions selected, both the single-quantum transition seen in the EDNMR spectra and the corresponding Davies ENDOR spectra are very similar, albeit slightly broader; the only difference is that EDNMR also resolves a sharp signal centered at the Larmor frequency of ^{17}O, corresponding to weakly coupled (second shell) water molecules associated with the Mn^{II} ion (see asterisks). This weakly coupled water signal is suppressed in the Davies ENDOR experiment due to blind spotting but can be readily observed in the corresponding Mims ENDOR experiment. All traces shown in Figure 3 panels D, E, and F were collected for the same time period, with approximately the same frequency step, yielding a sensitivity of EDNMR for this system 20-fold higher than for Davies ENDOR. As the ^{17}O signals for metalloproteins such as the OEC are expected to be much weaker than in model compounds, recourse to the EDNMR technique for these
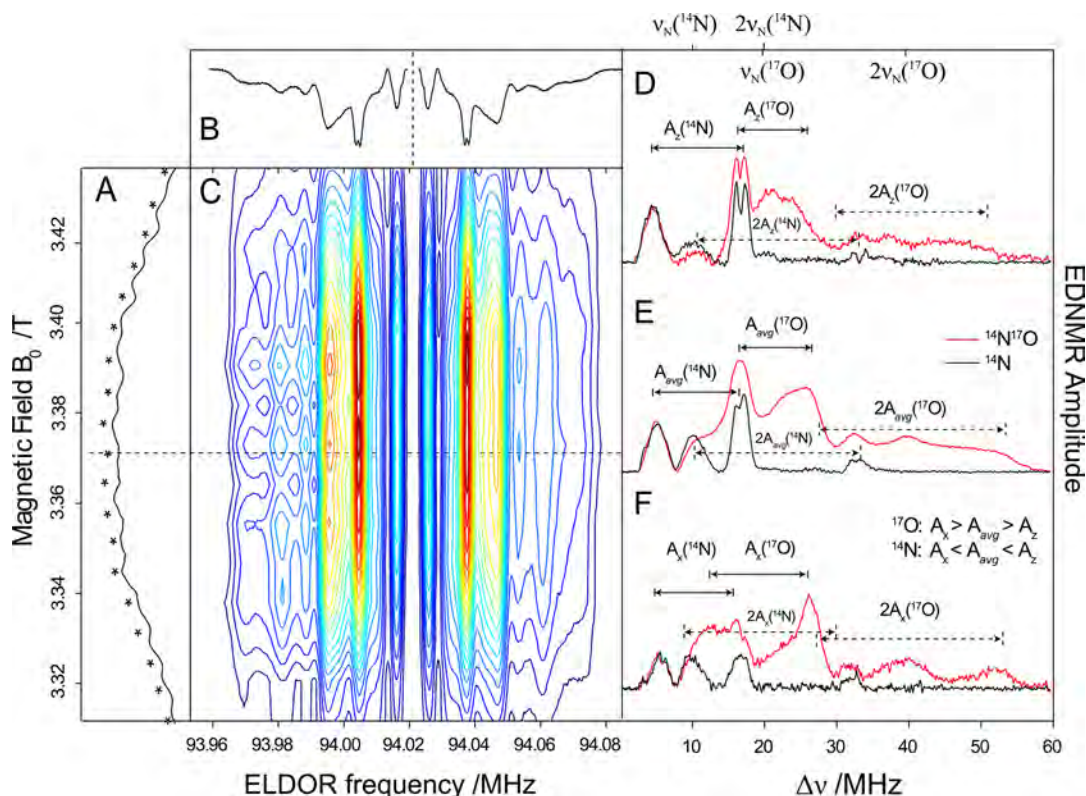
Figure 4. W-band EDNMR spectra of ^{17}O-labeled Mn^{III}−(μO)−−Mn^{IV} BIPY complex. (A) The EPR spectrum of the complex. (B) The EDNMR signal. (C) 2D EDNMR surface. (D−F) The EDNMR signals seen for the ^{17}O-labeled complex at three field positions (red lines) compared to those of unlabeled complex (black lines) collected at (D) the high field edge 3.44 T, (E) the central field 3.37 T, and (F) the low field edge 3.30 T.

systems may be necessary, especially for orientation selectivity measurements. These measurements require data collection on the edges of the signal profile (i.e., S_2 multiline signal), where signal intensities are often vanishingly small. As a final note, it is seen that the intensity of the ^{17}O matrix and double-quantum lines in the EDNMR experiment can be enhanced by varying the amplitude (ω_1) of the HTA pulse (see Figure 3E, I: ω_1 = 1.8 × 10^6, vs II: ω_1 = 0.8 x10^6 rad·s^{-1}).

3. RESULTS

3.1. ^{17}O-EDNMR of μ-Oxo Bridges in a Model System.

Mixed valence Mn dimer complexes have been historically used to calibrate measurements performed on the OEC of PSII. These complexes are considered "good" spectroscopic models as they typically display the same electronic ground state (S = $^1/_2$) and thus their multiline EPR spectrum is comparable to that seen for the half-integer paramagnetic states of the OEC, that is, S_0 and S_2.[63−72] In this way, a magnetic fingerprint of different Mn ligand motifs can be developed. The approach of using Mn dimer complexes as electronic structure mimics has been previously employed for benchmarking ^{55}Mn-ENDOR,[68−72] ^{14}N-ESEEM,[73−75] and ^{13}C-ENDOR[76] studies on the OEC. One particular ligand motif, the μ-oxo bridge, has been little studied.[47] The section below briefly demonstrates the capabilities of ^{17}O-EDNMR as applied to the model complex [$Mn^{III}Mn^{IV}(\mu$-$O)_2BIPY_4$]ClO_4,[77−79] BIPY = bipyridine, which was previously studied by Usov et al.[47] using ^{17}O-ENDOR. It is shown that this technique allows a complete characterization of the μ-oxo bridge motif and the structural factors that influence it.

The EDNMR surface of the ^{17}O-labeled mixed valent planar Mn^{III}−$(\mu O)_2$−Mn^{IV} BIPY complex[77−79] is shown in Figure 4.

The ^{17}O label was incorporated via isotope exchange with ^{17}O-labeled water. The final complex contained approximately 75% ^{17}O bridges, that is, in the majority of complexes both μ-oxo bridges were exchanged. The control ^{16}O-BIPY complex data are shown in black in Figure 4 panels D−F, resolving signals attributable to a ^{14}N ligand. Both single- and double-quantum transitions are observed. The single-quantum transitions are centered about the Larmor frequency of ^{14}N [$\nu_N(^{14}N)$ = 10.37 MHz, 3.37 T], split by the hyperfine coupling (full arrow in Figure 4 panels D−F), while double-quantum ^{14}N transitions are centered at twice the Larmor frequency of ^{14}N [$2\nu_N(^{14}N)$ = 20.74 MHz, 3.37 T] and split by twice the hyperfine coupling (dashed arrows in Figure 4 panels D−F). The ^{14}N peaks are narrow with peak widths of full width at half-maximum (fwhm) 3 MHz. This signal represents the strongly coupled ^{14}N axial ligand of the Mn^{III} ion that sits along its Jahn−Teller axis.[63] The remaining equatorial ^{14}N ligands of the Mn^{III} and all ^{14}N ligands of the Mn^{IV} are only weakly coupled and appear as a "matrix" line centered at the ^{14}N Larmor frequency. A further splitting of 1.2 MHz of the ^{14}N signal is observed for the EDNMR spectrum measured on the high field edge. This splitting is tentatively assigned to a quadrupole coupling of 2 MHz.

The corresponding ^{17}O-labeled BIPY complex data are shown in red in Figure 4 panels D−F. The single-quantum ^{17}O transitions appear as a broad doublet centered about the Larmor frequency of ^{17}O [$\nu_N(^{17}O)$ = 19.46 MHz, 3.37 T]. The two peaks of the doublet are best resolved when the EDNMR spectrum is measured on the low-field edge (Figure 4F). When measured on the high-field edge (Figure 4D), the two peaks of the doublet strongly overlap. The center field EDNMR

spectrum represents an average of the two edge spectra (Figure 4E). The ^{14}N and ^{17}O signals were simulated using the spin Hamiltonian formalism, see the Supporting Information, S7. The large difference seen between the low-, high-, and center-field spectra of the ^{17}O signal suggests that the hyperfine tensor is not axial but rather has a high degree of rhombicity. The fit requires that the anisotropic hyperfine coupling ($A_{dip} \sim 5$ MHz) to be of the same magnitude as the isotropic hyperfine coupling ($A_{iso} \sim 8$ MHz). These parameters serve as a preliminary magnetic fingerprint for a Mn μ-oxo bridge, namely, that the ^{17}O-hyperfine tensor of the bridge should display (i) a large isotropic coupling ~ 8 MHz and (ii) a hyperfine anisotropy that is large and highly rhombic.

3.2. ^{17}O-EDNMR-Based Detection of Water-Exchangeable Ligands of the Mn$_4$O$_5$Ca Cluster.

EDNMR presents the same advantages seen in model complexes for detection of ^{17}O coupling to the OEC. As seen for the BIPY model complex, the OEC is expected to exhibit at least one nitrogen signal from a coordinating histidine residue (D1-His332), seen in the X-ray crystal structure. As such, it is important to carefully characterize this ^{14}N species prior to performing the ^{17}O-labeling experiment. It will be shown later that this nitrogen signal also serves as a basis for assigning ^{17}O signals, as its geometric position within the OEC is known. As a final note, it is important to perform the ^{17}O-labeling experiments on approximately the same time scale as observed for substrate exchange. Long incubations in labeled water may lead to exchange of structural oxygens: oxygen ligands of the manganese cluster that are not substrate sites. This last point is detailed in Section 3.4.

3.2.1. EDNMR of the Nitrogen Signal of the D1-His332 Ligand of the Mn$_4$O$_5$Ca Cluster. W-band EDNMR spectra of ^{14}N-PSII and universally labeled ^{15}N-PSII, resuspended in unlabeled water and poised in the S$_2$ state are shown in Figure 5. The EDNMR spectrum of ^{14}N-PSII (Figure 5A, black trace) resolves a doublet centered about the Larmor frequency of ^{14}N [$\nu_N(^{14}$N$) = 10.46$ MHz, 3.4 T] with a peak-to-peak spacing of 7.0 MHz and a peak width fwhm of 2.5 MHz. A corresponding doublet is seen for ^{15}N-PSII (Figure 5C, black trace), but shifted to higher frequency, now centered about the Larmor frequency of ^{15}N [$\nu_N(^{15}$N$) = 14.68$ MHz, 3.4 T] with a peak-to-peak spacing of 9.7 MHz and a peak width fwhm of 2.5 MHz. These signals were absent in spectra of the S$_1$ state recorded using the same conditions. In contrast to the BIPY data (Figure 4), no quadrupole splitting was observed in the ^{14}N-PSII spectra. Double-quantum transitions for the ^{14}N-PSII sample were also observed. These were best visualized by increasing the length of the HTA pulse by an order of magnitude. This also enhances the matrix line, centered at the ^{14}N Larmor frequency (Figure 5A, lower black trace, II). A nitrogen species of approximately the same coupling (~ 7 MHz) was previously observed using Q-band ESEEM, in samples prepared from higher plant and cyanobacterial (*Synechocystis*) PSII by the Britt laboratory.[74,75,80] It was assigned to the D1-His332, which is the only nitrogen ligand that directly coordinates a Mn of the OEC (Mn$_{D1}$), see Figure 1.

3.2.2. Exchangeable Water-Derived Ligands of the Mn$_4$O$_5$Ca Cluster. W-band EDNMR spectra of ^{14}N-PSII and universally labeled ^{15}N-PSII, resuspended in H$_2^{17}$O and poised in the S$_2$ state are also shown in Figure 5A and C (red traces). In these samples, an additional signal is observed centered at the Larmor frequency of ^{17}O [$\nu_N(^{17}$O$) = 19.63$ MHz, 3.4 T].
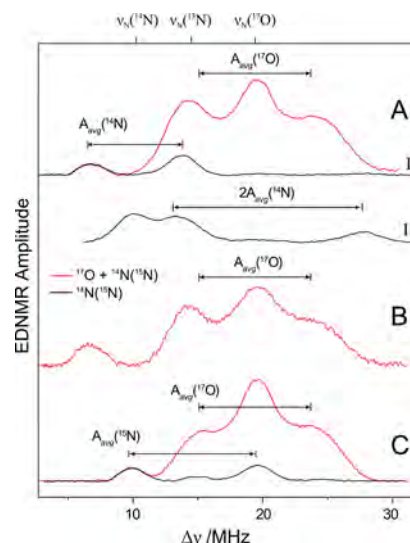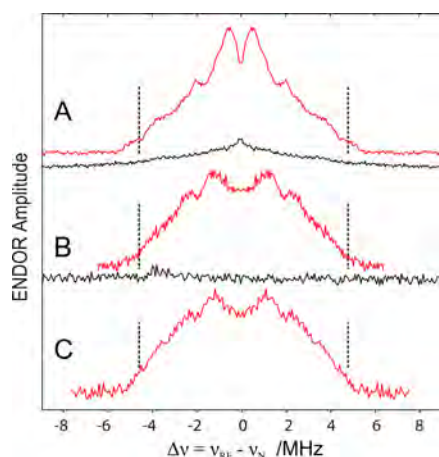

Figure 5. W-band EDNMR spectra of ^{14}N(^{15}N)-PSII poised in the S$_2$ state measured at the center of the multiline spectrum ($B_0 = 3.40$ T). (A) ^{14}N-PSII resuspended in unlabeled water (black) /H$_2^{17}$O (red). (B) ^{14}N-PSII rapidly diluted (15 s) in H$_2^{17}$O. (C) ^{15}N-PSII resuspended in unlabeled water (black) /H$_2^{17}$O (red). For (A), the EDNMR traces (black) were measured using HTA pulses optimal for (I) single quantum ^{14}N and (II) double quantum ^{14}N signals. For further sample information and all instrumentation parameters see Section 2, Materials and Methods.

The new signal observed upon ^{17}O enrichment consists of three peaks, a central line centered at $\nu_N(^{17}$O$)$, and two satellite lines appearing symmetrically about this position. The central line represents weakly coupled (matrix) exchangeable ^{17}O species associated with the OEC whereas the two satellite lines represent one or more exchangeable Mn–O ligands. The peak positions of the signal do not change between the ^{14}N- and ^{15}N-labeled samples, but the line intensities do vary. This is due to the different contributions of ^{14}N(^{15}N) signal described above. Subtraction of the ^{14}N(^{15}N) signal approximately results in the same line shape for the two sample types. The corresponding ^{17}O-Davies ENDOR spectrum was also recorded and is shown in the Supporting Information, S8. Double-quantum transitions are also observed for the ^{17}O-signal envelope, centered about twice the Larmor frequency of ^{17}O (see Figure 7A). The structure of the double-quantum envelope suggests there are at least two exchangeable oxygen nuclei coupled to the OEC. This second oxygen, which has an intermediate hyperfine coupling, is not resolved in the single-quantum envelope due to spectral congestion. Further experiments (NH$_3$ addition, magnetic field dependence) shown below (Section 3.2.4) demonstrate this is indeed the case. The ^{17}O-signal profile seen in PSII has approximately the same width as the ^{17}O-signal profile observed for the BIPY model complex described above (see Figure 4E).

Corresponding S$_2$ state field-sweep W-band EPR spectra of the OEC of ^{14}N-PSII and universally labeled ^{15}N-PSII, resuspended in buffer solutions made with either unlabeled water or H$_2^{17}$O are shown in the Supporting Information, S5. They displayed the typical unstructured S$_2$ multiline signal centered at $g \sim 1.976$, of width (fwhm) 90 mT.[81]

3.2.3. Protonation State of Oxo-Bridges of the Mn$_4$O$_5$Ca Cluster. The protonation state of the exchangeable water ligands identified above can be probed using ^{1}H/^{2}H-ENDOR spectroscopy. Figure 6 shows the ^{1}H Davies and corresponding

Figure 6. Proton/deuteron ENDOR spectra of ^{14}N-PSII of *T. elongatus* poised in the S_2 state measured at the center of the multiline spectrum (1.2 T). (A) Q-band ^{1}H-Davies-ENDOR, S_2 (red), S_1 (black). (B) Q-band ^{2}H-Mims-ENDOR, S_2 (red), S_1 (black). (C) W-band ^{2}H-Mims-ENDOR, S_2 (red). All signals are centered at the appropriate ^{1}H/^{2}H Larmor frequency. The frequency axis of the ^{2}H data sets are scaled to the ^{1}H frequency axis for easy comparison.
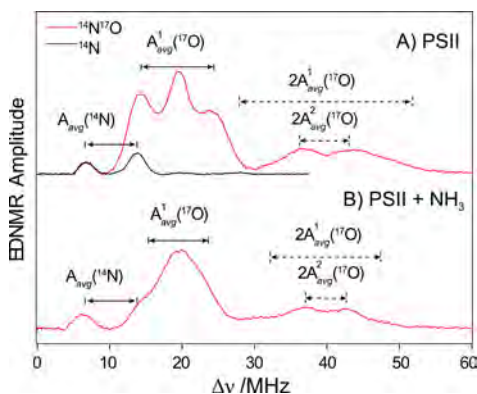
Figure 7. W-band EDNMR spectra of PSII poised in the S_2 state measured at the center of the corresponding EPR spectrum. (A) ^{14}N-PSII resuspended in unlabeled water (black) and $H_2{}^{17}$O (red). (B) ^{14}N-PSII + NH$_3$, resuspended in $H_2{}^{17}$O (red). Experimental/instrument parameters are listed in the Materials and Methods section.

^{2}H-Mims ENDOR spectrum of the OEC of *T. elongatus* poised in both the S_1 and S_2 states. The spectra were symmetrized about the Larmor frequency of the ^{1}H/^{2}H nucleus [$\nu_N(^1H) = 51.94$ MHz, $\nu_N(^2H) = 7.97$ MHz at $B_0 = 1.22$ T]. All raw data is given in the Supporting Information, S6. The width of the ^{1}H/^{2}H envelope is essentially the same as reported in earlier studies of higher plants. The magnitude of the hyperfine couplings observed are consistent with coordinating terminal water/hydroxyl ligands but are too small to represent a hydroxo-bridge species. This is demonstrated in the Supporting Information using the Umena et al.[1] crystal structure coordinates and the current electronic model for the OEC.[20,82] Electron−nuclear dipolar hyperfine coupling estimates (dipolar) for the ^{1}H nuclei for all "water" molecules identified within 5 Å of the OEC are listed in the Supporting Information, S9 and S10, along with a simulation of the ^{1}H/^{2}H envelope using these calculated values, see S11.

### 3.2.4. Experimental Verification of Three Classes of Exchangeable Water−Mn Couplings.

Beck et al.[83] demonstrated that NH$_3$ modifies the electronic structure of the Mn cluster poised in the S_2 state. Britt et al.[73] subsequently showed using ESEEM that NH$_3$ binds to the OEC in samples prepared from higher plants poised in the S_2 state (A_{iso} = 2.29 MHz). Curiously, NH$_3$ does not bind to the OEC in the S_1 state. Similar results have been observed in thermophilic cyanobacteria,[84] which is the PSII material used in this study. While it remains unclear what the exact action of NH$_3$ is and how many binding sites it has at/near the Mn$_4$O$_5$Ca cluster, one role proposed for this water analogue is that it displaces or modifies a manganese-bound water substrate.

Here, we have tested this proposal by adding ammonia to dark adapted (S_1-state) $H_2{}^{17}$O-exchanged PSII samples. Upon illumination at temperatures below 190 K,[85] the typical S_2 state EPR multiline signal was seen in control samples using Q-band EPR. In addition, W-band EDNMR measurements resolve the same ^{17}O-signal profile, demonstrating NH$_3$ does not bind to or modify the S_1 state. As shown previously by Boussac et al.,[85] subsequent annealing of the sample to 250 K allows NH$_3$ to interact with the S_2 state of the OEC (Figure 7B). In the EDNMR experiments reported here, annealing led to a narrowing of the ^{17}O-signal envelope (single quantum), with the two satellite lines seen at 14.2 and 23.8 MHz shifting toward the ^{17}O Larmor frequency. The remaining single-quantum envelope was only ∼6 MHz broad. The change observed for the double-quantum envelope is more complicated. Consistent with the narrowing seen for the ^{17}O single-quantum envelope, the broad edges do contract by ∼6 MHz (i.e., twice the contraction seen for the single-quantum satellites). In contrast however, the peaks observed at about twice the ^{17}O Larmor frequency are retained and only slightly narrowed (∼1−2 MHz). This differential behavior demonstrates that the observed ^{17}O-signal envelope must be composed of at least three components. It contains (i) a strongly coupled species, with ^{17}O-hyperfine coupling of ∼10 MHz, representing a Mn-bound ^{17}O species; (ii) an intermediately coupled species, with ^{17}O-hyperfine coupling of ∼5 MHz, representing a second Mn-bound ^{17}O species, which is hidden in the single-quantum envelope due to spectral congestion; and (iii) more weakly coupled matrix water molecules of unresolved hyperfine coupling, which manifest as the central line observed at the Larmor frequency.

The magnetic field dependence of the EDNMR signals provides further information about the identity of exchangeable water ligands, as seen for the model complex in Section 3.1. The ^{17}O-signal profile seen for the OEC also exhibits a small, but observable magnetic field dependence (2−3 MHz, Figures 8 and 9). The exact peak separation of the single-quantum satellite peaks (14.2 and 23.8 MHz) increases as the magnetic field increases. This is best resolved at the high-frequency edge as this feature does not overlap with the ^{14}N signal. As before, the behavior of the double-quantum signal is more complicated. The edges of the double-quantum envelope are not well-resolved across the whole EDNMR surface but do appear to follow the trend seen for the single-quantum envelope. This is in contrast to the narrow component. The splitting of its peaks (37.0 and 43.5 MHz) instead decreases measured across the multiline spectrum. This is further evidence that the ^{17}O-EDNMR signal envelope contains two large ^{17}O couplings (>4 MHz), consistent with the NH$_3$ experiment described above. It is noted that the ^{14}N(^{15}N) signal also displayed a weak magnetic field dependence (∼1.5 MHz), with the smallest hyperfine splitting for the EDNMR spectrum measured on the low-field edge of the EPR signal. The same field dependence is
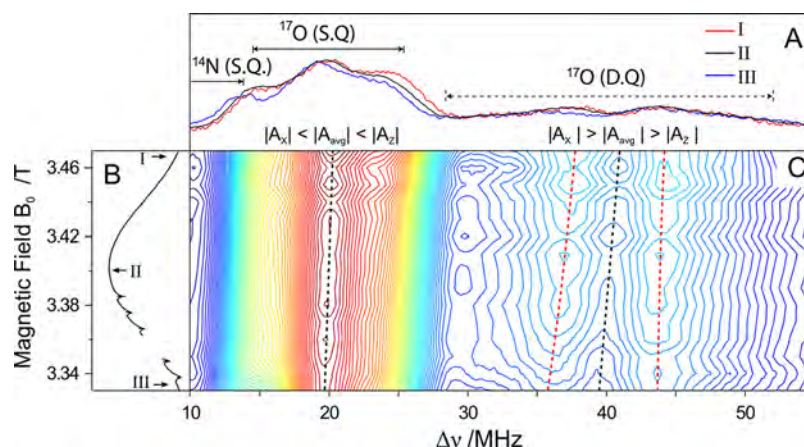
Figure 8. W-band 2D-EDNMR surface of ^{14}N-PSII poised in the S$_2$ state, resuspended in H$_2$^{17}O in the S$_1$ state. (A) EDNMR spectra measured at the high-field (I: 3.47 T, red), center (II: 3.40 T, black), and low-field (III: 3.33 T, blue) edge of the multiline spectrum. (B) The EPR multiline spectrum. (C) The 2D EDNMR representation of (A). The black dashed lines show the magnetic field dependence of the single-quantum and double-quantum ^{17}O-Larmor frequency. Lines locating the average peak separation of the narrow component of the double-quantum envelope are also shown (red dashed line). Experimental/instrument parameters are listed in the Materials and Methods section.
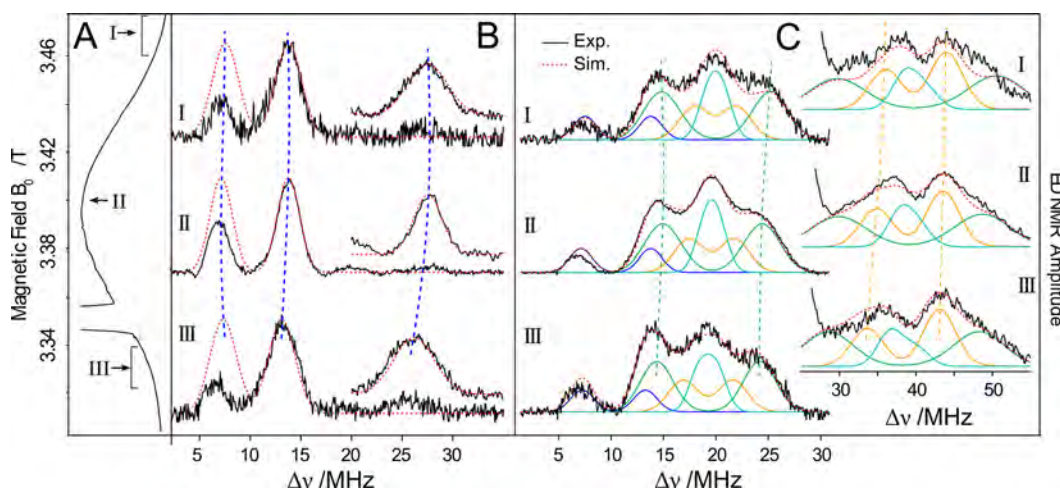
Figure 9. Spin Hamiltonian simulations of the ^{14}N and ^{17}O signals seen for the OEC. (A) A representative S$_2$ multiline spectrum. (B,C) Simulation of the single (left) and double quantum (right) ^{14}N/^{17}O-EDNMR signal envelopes at three field positions: (I) the high-field edge (3.46−3.47 T); (II) the center (3.40 T); and (III) the low-field edge (3.33−3.34 T). Spin Hamiltonian parameters are listed in Table 1. Dashed lines show the field dependence of the respective EDNMR peaks.

Table 1. ^{14}N and ^{17}O Hyperfine Spin Hamiltonian Parameters, Comparison to Calculated Parameters for the 1d2′ Model of Ames et al.[19] (Figure 1B)^a

		spin Hamiltonian parameters (MHz)						DFT (MHz)	
		A_x	A_y	A_z	A_{iso}	A_{dip}	$A(\eta)$	A_{iso}	site
BIPY	N (JT)	10.8	11.3	12.5	11.5	0.5	0.52	−	−
	μO	18.0	−0.8	6.8	8.0	5.0	0.76	−	−
D1-His332	^{14}N	3.8	7.7	6.2	5.9	1.1	0.71	−5.2	His332
^{17}O envelope	strong	10.7	5.2	13.1	9.7	2.2	0.54	−	−
	interm.	5.0	5.1	3.3	4.5	0.6	0.09	−4.7	W2
	matrix	2.1	0.2	2.0	1.4	0.6	0.08	−1.5	W1

^{a}A_{iso} is defined as the average of the principal components of the hyperfine tensor: $A_{iso} = (A_x + A_y + A_z)/3$. A_{dip} is defined in terms of T_1, T_2, and T_3 as $A_{dip} = (T_1 + T_2)/2 = -T_3/2$, and the rhombicity is as defined by $\eta = (T_1 - T_2)/T_3$. T_1, T_2, and T_3 represent the three principal components of the hyperfine tensor minus A_{iso} and labeled such that $|T_1| \leq |T_2| \leq |T_3|$. The ^{14}N hyperfine tensor was rotated 30° in the g_X/g_Z frame: $[\alpha\ \beta\ \gamma] = [0\ 30°\ 0]$.

observed for the ^{14}N double-quantum signal at 26−28 MHz (see Figure 9).

3.3. Assignment of ^{17}O-EDNMR Signals—Spin Hamiltonian Simulations. Spectral simulations of the ^{17}O-signal envelope inclusive of both single- and double-quantum transitions were performed using the spin Hamiltonian formalism (for details see Section 2.5 and the Supporting Information, S7). Spectral simulations of the ^{17}O-EDNMR signal envelope measured for ^{14}N-PSII are shown in Figure 9. Simulation of the EDNMR surface ensured that correct

estimates were made for both the isotropic and anisotropic components of the ^{17}O-hyperfine tensors.

A simulation of the ^{14}N signal using similar spin Hamiltonian parameters as reported by Stich et al.[74] is shown in Figure 9. A small decrease in the A_{iso} of 10% and consequently an increase in A_{dip} was required to reproduce the field dependence, see Table 1. The simulation places the unique principal axis of the ^{14}N-hyperfine tensor approximately along g_x, that is, it coincides with powder pattern orientations that define the low-field edge of the EPR (multiline) spectrum. The best fit to the data included a 30° rotation of the hyperfine tensor in the g_x/g_z frame (see the Supporting Information, S12 and S13 for further details).

As described in the previous section, the fitted ^{17}O-signal envelope requires three oxygen species: one strongly coupled oxygen species, one intermediately coupled oxygen species, and weakly coupled "matrix" oxygen species. Figure 9 represents an unrestricted fitting to the ^{17}O-EDNMR surface data that includes three ^{17}O-hyperfine couplings. All ^{17}O-hyperfine tensors were forced to be collinear with the molecular g-tensor. Spin Hamiltonian parameters are given in Table 1. An alternative restricted fitting of the ^{17}O-EDNMR data using crystal structural constraints is shown in the Supporting Information, S10, S12, and S13. Both approaches yield basically the same result. Assignments for the three ^{17}O oxygens are as follows:

(1) A Mn μ-oxo bridge. The fitted hyperfine tensor of the first species has an isotropic hyperfine coupling of A_{iso} = 9.7 MHz and an anisotropic coupling of A_{dip}= 2.2 MHz of large rhombicity $\eta \sim 0.6$. These parameters broadly match those seen for the μ-oxo bridges of the Mn^{III}–$(\mu O)_2$–Mn^{IV} model complex shown in Section 3.1, and thus, this oxygen is assigned to a μ-oxo bridge. A rationale for the apparent decrease in hyperfine anisotropy is given in the discussion and in part serves to identify the μ-oxo bridge (see the Discussion section). This component of the ^{17}O-signal envelope is broadly consistent with the signal seen in the study of McConnell et al.,[46] which was also assigned to a μ-oxo bridge.

(2) A terminal Mn–water/hydroxo ligand. The fitted hyperfine tensor of the second species has an isotropic hyperfine coupling of A_{iso} = 4.5 MHz and an anisotropic coupling of A_{dip}= 0.6 MHz with rhombicity $\eta \sim 0.1$. These parameters do not match well with those determined for the μ-oxo bridges of the Mn^{III}–$(\mu O)_2$–Mn^{IV} model complex, shown in Section 3.1; both the isotropic and anisotropic hyperfine components are significantly smaller. However, these parameters do match ^{14}N-hyperfine couplings seen for terminal nitrogen Mn^{IV} and equatorial Mn^{III} ligands in mixed valence model complexes[73,86] (see the BIPY complex above). As such, the second species is assigned to one or both of the terminal water/hydroxo ligands of Mn$_{A4}$. The more axial nature of the hyperfine tensor associated with this oxygen is consistent with this assignment.

(3) Matrix water. The "3rd oxygen", or rather a collection of oxygen species, which defines the central line describes weakly coupled "matrix" water. The fitted isotropic hyperfine coupling is $A_{iso} \sim 1$–2 MHz which suggests one component of the matrix line describes a ligand to a manganese, that is, Mn–OH$_2$. Very weak couplings within this envelope can be extracted using an alternative

technique, W-band Mims-ENDOR (Supporting Information, S8). The Mims-ENDOR signal has a near Lorentzian line shape with a splitting of 0.5 MHz. Similar lineshapes albeit of enhanced resolution have been identified previously in ^{17}O-model systems, for example, weakly coupled H$_2$^{17}O-coordinating Gd^{3+} complexes.[87] As the simulation of the PSII ^{17}O-Mims ENDOR profile requires the inclusion of a nontrivial isotropic hyperfine coupling ($A_{dip} \sim A_{iso} = 0.25$ MHz), we favor assigning this signal to the OEC/Ca bound waters W3 and W4, (see the Supporting Information, S8) as opposed to noncoordinating waters in the vicinity of the OEC. However, we cannot exclude a significant contribution to the envelope from surrounding waters of the second coordination sphere, particularly those near Mn$_{D1}$ (see the Supporting Information, S8 and S11.1).

DFT calculations were performed to validate the above assignment of the ^{17}O-EDNMR envelope (see the Supporting Information, S14). Currently, Broken symmetry (BS)-DFT estimates for the isotropic hyperfine coupling of the five μ-oxo bridges of the Mn$_4$O$_5$Ca cluster cannot be made. Thus, only estimates for the terminal Mn–OH/OH$_2$ ligands and more distant Ca–OH$_2$ ligands are reported. The structural model used was the previously published 1d2′ model of Ames et al.[19] (see Figure 1B). DFT calculated hyperfine values for W1–W4 are all less than 5 MHz (Table 1), significantly smaller than the largest measured hyperfine coupling (10 MHz), suggesting this large coupling does indeed arise from another Mn–O ligand motif, that is, a μ-oxo bridge of the Mn$_4$O$_5$ core complex. In addition, the DFT hyperfine values for W2 and W1 appear to correlate with the experimental intermediate and weak coupling components of the fitted EDNMR signal envelope: W2, a terminal hydroxide ligand coordinated to Mn$_{A4}$ in the 1d2′ model, has a calculated hyperfine coupling of 4.7 MHz; and W1, a terminal water ligand coordinated to Mn$_{A4}$ in the 1d2′, has a calculated hyperfine coupling of 1.5 MHz. The remaining waters W3/W4, water ligands to the Ca, are all predicted to display small hyperfine couplings (~ 0.1 MHz). This is consistent with the Mims-ENDOR signal envelope observed (see the Supporting Information, S8).

3.4. Water Exchange Rates. To test whether the ^{17}O signal(s) described in the previous section are potential candidates for the substrate bound in the S$_1$/S$_2$ state, further experiments were performed in which the PSII core complexes poised in the S$_1$ state were rapidly diluted into H$_2$^{17}O buffer (see the Materials and Methods section). The PSII sample was diluted by 50% with H$_2$^{17}O water, frozen to 77 K, and then, illuminated with white light for 5 s at 200 K to generate the S$_2$ state. The time resolution of the experiment, that is, the minimum mixing and incubation time of the PSII sample in H$_2$^{17}O buffer prior to freezing, was less than 15 s. The exchange rate of the slowly exchanging substrate molecule has been measured by membrane inlet mass spectrometry to be in the order of 0.066 s^{-1} ($t_{1/2}$ = 10 s) at 20 °C; thus, this period of time should be sufficient to significantly exchange substrate water molecules in the S$_1$ state.[10,22−24,107] Figure 5B (red trace) shows the ^{17}O-EDNMR signal observed in samples prepared using this protocol. It is readily seen that approximately the same ^{17}O-signal envelope is observed as in Figure 5A. The corresponding double-quantum transitions are shown in the Supporting Information, S8.3. As expected, the intensity of the entire signal, relative to the ^{14}N (D1-His332) signal, is lower

16628

dx.doi.org/10.1021/ja3053267 | J. Am. Chem. Soc. 2012, 134, 16619−16634

than in the resuspended sample as the final [17]O enrichment is lower, a maximum of 45% versus >70%. Thus, all detected [17]O signal(s) exchange within 15 s, that is, on the same time scale as substrate water. A more robust exchange procedure with enhanced time resolution is currently being developed in our laboratory to provide a quantitative estimate of the exchange rate(s) of the three exchangeable oxygen species.

4. DISCUSSION

4.1. General Remarks. In this study, an attempt has been made to develop a new experimental approach to solve one of the most important remaining questions regarding the function of the OEC, substrate water binding. The two-step program described above, where both model complexes and the OEC were studied, places new important constraints on the structure and function of the OEC. Multiple [17]O signals are resolved, demonstrating the complex interplay of the OEC with the solvent background, which uniquely also forms the substrate for the catalyst. Furthermore, all spectroscopic parameters measured for the ^{1}H/^{14}N nuclei associated with the OEC are consistent with current literature models for the electronic structure of the OEC,[20,68,82] a tetramer, where all four Mn are coupled and contribute approximately equally to the ground electronic state. In the following discussion, preliminary assignments are proposed for the [17]O signals observed.

4.2. μ-Oxo-[17]O Model Complex Data. Only one study exists in the current literature that describes a [17]O nucleus coupled to a high valent (Mn[III], Mn[IV]) model complex, namely, the BIPY complex, the same as studied here.[47] In this earlier work, a broad, structureless [17]O signal was seen using Q-band ENDOR centered at ∼12 MHz. An estimate of the isotropic coupling was made (A_{iso} ∼13 MHz) from the center of the peak of the signal (+ branch), which was shown to be consistent with the observed line broadening seen in the corresponding the cw-EPR experiment. No estimate was reported for either the hyperfine anisotropy or quadrupole splitting. An isotropic coupling estimate of A_{iso}∼13 MHz is somewhat larger than the value reported here, A_{iso}∼8 MHz. The difference is suspected to arise from a feature of the ENDOR experiment. Q-band ENDOR is often not particularly sensitive at very low frequencies where much of the [17]O-signal envelope is expected when measured at 34 GHz. Thus, the signal peak observed does not represent a true average coupling but is instead skewed toward higher frequencies overestimating the isotropic coupling. The same problem is not encountered using W-band EDNMR.

The key advantage of W-band EDNMR for [17]O-model complexes of this type is that it allows the hyperfine anisotropy to be estimated, thus allowing a characteristic fingerprint of the μ-oxo bridge to be developed. As noted in Section 3.1, the strong field dependence of the width of the [17]O signal, where the low-, high-, and center-field spectra all have a different width, suggest the hyperfine anisotropy is large and that the tensor is not axial but rather has a high degree of rhombicity. Spectral simulations (shown in the Supporting Information, S7), using the spin Hamiltonian formalism, are consistent with this description (A_{iso} ∼ 8 MHz, A_{dip} ∼ 5 MHz). The hyperfine tensor is aligned such that its largest and smallest components (in terms of signed magnitude) are along g_x and g_y (or at least are orientated in the g_x/g_y plane) whereas the middle component is aligned along g_z. This result can be well understood within the current model for strongly antiferromagnetically coupled Mn[III]Mn[IV] dimers (J < −100 cm^{−1}). In

these systems, the Jahn−Teller axis of the Mn[III] ion defines the unique axis (g_z axis) of the system.[88] It is aligned along the Mn[III]−N bond perpendicular to the plane defined by the Mn−(μO)$_2$−Mn atoms. The large hyperfine anisotropy of the [17]O bridge (5 MHz) comes about from the through space (dipolar) interaction between the ligand and the two Mn ions; the electron−nuclear dipolar hyperfine coupling estimate for the μ-oxo bridge is 4.5 MHz (see the Supporting Information, Table S10.7). The measured (projected) [17]O-dipolar hyperfine interaction is a weighted sum of the two onsite [17]O-dipolar hyperfine tensors that describe the interaction of the [17]O nucleus with either the Mn[III] or Mn[IV]. The relative contribution of each onsite [17]O-hyperfine tensor depends upon the contribution of the Mn[III] and Mn[IV] ions to the electronic state of the complex, which is often described in terms of a spin projection coefficient, see refs 89 and 90. For the antiferromagnetically coupled Mn[III]Mn[IV] dimer, $S_{1(MnIII)}$ = 2, and $S_{2(MnIV)} = {}^3/_2$ the spin projection values are ρ_1 = 2 and ρ_2 = −1, respectively. The tensor sum is shown as a diagram in Figure 10.
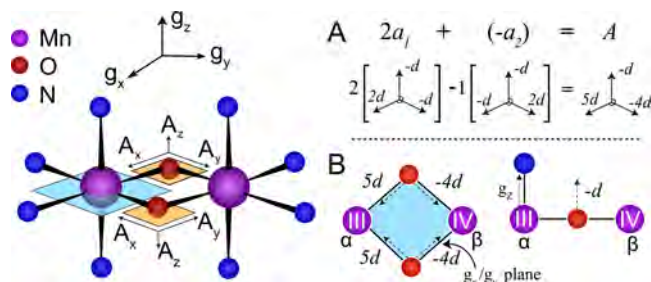
Figure 10. Dipolar hyperfine tensor of the μ-oxo bridge of an antiferromagnetically coupled Mn[III]Mn[IV] dimer. (A) Onsite (individual) dipolar hyperfine tensor components in the Mn−O−Mn plane and perpendicular to the Mn−O−Mn plane. (B) Orientation of the projected (experimental) hyperfine tensor.

The two onsite [17]O-dipolar hyperfine tensors, which are expected to be approximately axial, yield a projected [17]O-dipolar hyperfine tensor that has about rhombic symmetry. The unique principal axis should be parallel to a plane that is defined by the Mn−(μO)$_2$−Mn bridging motif, whereas, the middle component (in signed magnitude) must be perpendicular to the Mn−(μO)$_2$−Mn bridging motif. This is exactly the behavior observed experimentally. The largest component (unique axis) of the [17]O-dipolar hyperfine tensor coincides with g_x/g_y, that is, the plane defined by the Mn−(μO)$_2$−Mn bridging motif, whereas the middle component of the [17]O-hyperfine tensor coincides with g_z, that is, perpendicular to the plane defined by the Mn−(μO)$_2$−Mn bridging motif.

4.3. Assignment of the μ-[17]O Bridge in the Mn$_4$O$_5$Ca Cluster. The model system described above provides a basis for the assignment of the exchangeable μ-[17]O bridge. Two parameters can be used: (i) the magnitude of the hyperfine anisotropy; and (ii) the orientation of the hyperfine tensor with respect to the three planes that describe the Mn−(μO)$_2$−Mn bridge network (see Figure 1).

As described above, the hyperfine anisotropy of Mn complexes is predominately due to a through space coupling mechanism and as such can be readily calculated for the oxo-bridges of the OEC. These calculations, termed multipole calculations, have been described in a number of papers, for example, ref 91. Its implementation here is described in the

Supporting Information, S9 and S10. The results are summarized in Table 2. Here, all Mn−^{17}O distances and ^{17}O

Table 2. ^{17}O−Mn Distances and Electron−Nuclear Dipolar Hyperfine Couplings for the μ-Oxo Bridges of the Umena et al.[1] Structure and a Recent Representative Computational Model of Ames et al.[19] (1d2′, Numbers in Brackets, see Figure 1) Using the Isotropic Spin Projections for the Model of Siegbahn (Model 11) Reported in Pantazis et al.[82]

	Mn−O Distances (Å)				
	Mn_{A4}−O−Mn_{B3}		Mn_{B3}−O−Mn_{C2}	Mn_{C2}−O−Mn_{D1}	
	O4	O5	O2	O1	O3
Mn_{A4}	2.1 (1.8)	2.5 (1.8)	3.8 (3.7)	5.2 (5.0)	4.7 (4.3)
Mn_{B3}	2.1 (1.8)	2.4 (1.9)	1.9 (1.8)	3.5 (3.4)	2.1 (2.0)
Mn_{C2}	4.5 (4.4)	3.8 (3.6)	2.1 (1.8)	2.1 (1.8)	2.1 (1.9)
Mn_{D1}	5.2 (5.0)	2.6 (3.0)	3.7 (3.6)	1.9 (1.8)	1.8 (1.9)
Projected ^{17}O-Hyperfine Tensors (MHz)					
$A_{dip}(^{17}O)^a$	1.8 (2.0)	2.0 (3.2)	1.2 (1.6)	3.5 (3.8)	4.0 (3.6)
$\eta(^{17}O)^b$	0.8 (0.9)	0.5 (0.7)	0.6 (0.4)	0.5 (0.7)	0.1 (0.2)

^{a}Principal value for the ^{17}O-hyperfine tensor: $A_{dip}(^{17}O) = (T_1 + T_2)/2 = -T_3/2$; $|T_1| \leq |T_2| \leq |T_3|$. ^{b}Rhombicity of the ^{17}O hyperfine tensor as defined by $\eta(^{17}O) = (T_1 - T_2)/T_3$; $|T_1| \leq |T_2| \leq |T_3|$.

electron−nuclear dipolar hyperfine coupling estimates are provided for the five μ-oxo bridges of the Umena et al.[1] structure and of a representative computational model of the recent DFT study of Ames et al.[19]

It is readily seen that the hyperfine anisotropy of all the μ-oxo bridges of the OEC is systematically lower than that of model complexes. This result is unsurprising as the spin projection coefficients for the four Mn ions are all smaller, falling in the range of 0.9−1.6, as now the electron spin is distributed across more Mn ions. The bridges that consist of a mixed valence pair of Mn ions (O1 and O3), those that best resemble the BIPY complex, have anisotropies approaching that of the model system. In contrast, the μ-oxo bridges between equivalent Mn ions (O2 and O4) have smaller anisotropies, between 50% and 75% of that seen for the model system. O5, which can equally be considered an elongated μ-oxo bridge between either Mn_{A4} and Mn_{B3} or Mn_{B3} and Mn_{D1} in the Umena crystal structure, more closely resembles the O2 and O4 (equivalent limit) than O1 and O3 (mixed valence limit). It should be noted though that, in optimized DFT structures, the position of O5 shifts such that it becomes a genuine μ-oxo bridge between Mn_{A4} and Mn_{B3}.[19] As the experimental (fitted) hyperfine anisotropy of the μ-oxo bridge is small (2.2 MHz), the μ-oxo bridges between the equivalent Mn atoms are the best candidates, that is, O2 and especially O4 and O5 (Figure 1). This is shown explicitly in the Supporting Information, S13.

The orientation of the μ-oxo bridge hyperfine tensor can then be used to refine the assignment of the μ-oxo bridge signal. This can be mapped to the three-dimensional structure of the OEC using the D1-His332 signal. It is seen from the EDNMR simulations that the unique principal axis of the μ-oxo bridge ^{17}O-hyperfine tensor coincides with powder pattern orientations that define the center of the multiline spectrum (aligned along g_y). This is in contrast to the D1-His332 signal. Its unique principal axis instead coincides with powder pattern orientations that define the low-field edge of the multiline spectrum (approximately aligned along g_x). Thus, the two hyperfine tensors must be rotated by 90° to each other. The orientation of the unique principal axis of the ^{14}N(^{15}N) D1-

His332 should lie along the Mn_{D1}−N bond as the magnitude of its hyperfine anisotropy is consistent with a through space (dipolar) interaction. The orientation of the unique principal axis for each of the μ-oxo bridges can be determined from the multipole calculations and is given in the Supporting Information, S12 (Tables S12.1−S12.4). Importantly, it can be seen that the unique principal axis for all μ-oxo bridges lie in the respective Mn_X−(O)$_2$−Mn_Y plane (see Figure 1), as seen in model complexes. The only exception is the unique principal axis of O2. It is rotated out of the Mn_{B3}−O−Mn_{C2} plane, that is to say it is perpendicular to the Mn_{B3}−Mn_{C2} μ-oxo bridge plane. This is not surprising as the Mn_{B3}−O−Mn_{C2} couple is unlike the BIPY model systems; it has been determined from calculations that the exchange pathway between Mn_{B3} and Mn_{C2} is ferromagnetic.[19,82,92]

From inspection of Figure 1, it can be seen that the unique principal axis direction for bridges O2−O5 are all approximately perpendicular to the unique principal axis direction of the D1-His332. This is explicitly demonstrated in the Supporting Information, S12. A better restriction is to consider what component of the ^{17}O-hyperfine tensor is aligned (parallel) to the unique principal axis of the D1-His332 hyperfine tensor, that is, the Mn_{D1}−N bond. In the simulations, it was found that the middle component of the ^{17}O hyperfine tensor coincides with powder pattern orientations that define the low field edge of the multiline spectrum. In Figure 10 it can be seen that the middle component of the ^{17}O-hyperfine tensor is normal to the Mn−(μO)$_2$−Mn plane for an antiferromagnetically coupled dimer. Again, from inspection of Figure 1, it can be readily seen that the only Mn−(μO)$_2$−Mn plane whose normal is approximately parallel with the Mn_{D1}−N bond is the one containing O4 and O5 (orange plane) and thus must contain the exchangeable μ-oxo bridge (see the Supporting Information, S12). No further restriction can be made as O4 and O5 are arranged in a similar fashion relative to the Mn_{D1}−N bond. It is also noted that the Mn_{D1}−His332 ^{14}N signal[74,75] is not significantly perturbed by the binding of ammonia suggesting ammonia does not affect the ligand environment of the Mn_{D1} ion. This further supports the assignment of the exchangeable μ-oxo bridge to either O4 or O5 as these are the only bridges (along with O2) that are not ligands of Mn_{D1}.

4.4. Literature Evidence for an Exchangeable μ-Oxo Bridge—FTIR Spectroscopy and Mass Spectrometry. Low-frequency FTIR spectroscopy supports the above hypothesis that the OEC contains an exchangeable μ-oxo bridge. In the higher plant study of Chu et al.,[93] a Mn−O mode was identified in the S_2/S_1 difference spectrum, downshifting from 625 to 606 cm^{-1}. This mode also showed an isotope labeling effect, shifting 10 cm^{-1} in samples suspended in $H_2^{18}O$.[93] Similar results were also obtained for *T. elongatus* core preparations by Kimura et al.[94] Recently, it was demonstrated that this exchangeable μ-oxo bridge signal is not observed in NH$_3$-treated samples.[95] Unfortunately, as the FTIR experiments require long incubation times to reach thermal equilibrium, this signal could not be straightforwardly assigned to a potential substrate. Our rapid dilution exchange EDNMR experiments (Figure 5B) support such an assignment. By comparison of these PSII FTIR signals to data obtained with Mn (di-μ-oxo) and related Mn/Fe compounds, both in terms of the frequency of the vibrational mode and the magnitude of the isotope effect, this signal was assigned to a ν_{sym}(Mn−μO−Mn) bridge or potentially a μ_2-oxo, μ_3-oxo bridge. Interestingly, this mode was sensitive to Sr^{2+} substitution (upshift by 12

cm^{-1}) but insensitive to ^{44}Ca substitution.[93] Chu et al. used this finding to favor that the Sr-induced shift is due to an indirect structural change and not to a direct ligation of this μ-oxo bridge to Ca/Sr. However, EXAFS data by Pushkar et al.[18] and our recent EPR/ENDOR data (Cox et al.,[20] Lohmiller et al.[96]) show that no significant structural change is imparted to the Mn_4O_5 cluster by Ca/Sr substitution or even Ca depletion. It is therefore suggested that the above FTIR data indeed provide direct evidence for Ca/Sr ligation of the exchangeable bridge and that the significantly smaller vibrational shift to be expected from $^{40}Ca/^{44}Ca$ exchange was lost within the noise of the FTIR experiments. It is noted that, of the two bridging ligands that are considered candidates for an exchangable μ-oxo bridge, only O5 is a μ-oxo linkage of the Mn_4O_5 cluster to the Ca^{2+} ion and thus the observed shift induced by Sr^{2+} favors O5 as the exchangeable μ-oxo bridge. This assignment also seems to fit best with the exchange kinetics of the slowly exchanging substrate water (W_s) as determined by fast membrane inlet mass spectrometry.[48] The rate of exchange is significantly increased by replacement of the Ca ion with Sr,[21,22] favoring the Mn/Ca-bridging O5 as opposed to the non-Ca ion bridging O4 ligand.

4.5. Fast-Exchanging μ-Oxo Bridge. The demonstration that a Mn-Mn μ-oxo bridge of the OEC can exchange on a time scale similar to that of the substrate is novel. Similar fast exchange rates have not yet been observed in model systems[49] including a recent report for the superoxidized Mn catalase metallocofactor.[46] For synthetic complexes, dissolved in organic solvents, this difference in μ-oxo bridge exchange rates is perhaps unsurprising. These models lack several features of the OEC, such as nearby acid/base derivates that presumably couple oxygen inclusion with proton release/uptake. The same rationale cannot be applied to the slow exchange seen for the Mn catalase model as it contains many of these features. As such, it is unclear why the measured exchange rate of the μ-oxo bridge in this system is so slow. It should be noted though that the state characterized was the superoxidized state ($Mn^{III}Mn^{IV}$), which is not physiological. Similarly, the physiological states ($Mn^{II}Mn^{II}/Mn^{III}Mn^{III}$) of the cofactor do require the bridge to be exchangeable as one of the bridges represents the first substrate (HOOH) of the dismutation reaction. In addition, in the di-Mn catalase, the oxo-bridge is not connected to a Ca^{2+}/Sr^{2+} ion with terminal water ligands, and the hydration sphere of the Mn^{III} is smaller; it has one water ligand as opposed to two (see Figure 1, Mn_{A4}), and this water is located in a hydrophobic pocket. It has also been suggested that internal oxygen exchange between terminal water ligands to Ca (or Mn) may allow the relatively fast exchange observed for O5 (W_s).[49,97]

In the same study, on the Mn catalase, water/μ-oxo bridge exchange in the S_1 state of the OEC was examined. It was found that long incubations in $H_2{}^{17}O$ water were required to exchange a putative μ-oxo bridge signal, which is likely the same species observed in the present study. In addition, no fast-exchanging signals attributable to terminal bound Mn_{A4}—water/OH were reported. Both of these results do not agree with the findings presented in this manuscript. The latter observation is especially curious as in all model systems terminal water ligands exchange rapidly. At this point, we cannot offer a concrete explanation for this discrepancy.

4.6. Consequences for the Mechanism of Water Oxidation. The question of what catalytic reaction pathway the OEC employs to generate an O—O bond is essentially twofold. It requires both the identification of the two substrates sites and an understanding of the chemical mechanism via which these adjacent substrates couple together. Importantly, these two considerations are not mutually exclusive. The position of the substrate site(s) limits the chemistry that can occur and vice versa.

The chemical mechanism via which the two oxygen atoms couple together can be broadly grouped into two classes: (I) mechanisms that involve nucleophilic attack between two substrate oxygen atoms and (II) oxo/oxyl radical coupling of two Mn oxygen ligands (Figure 11). The nucleophilic attack
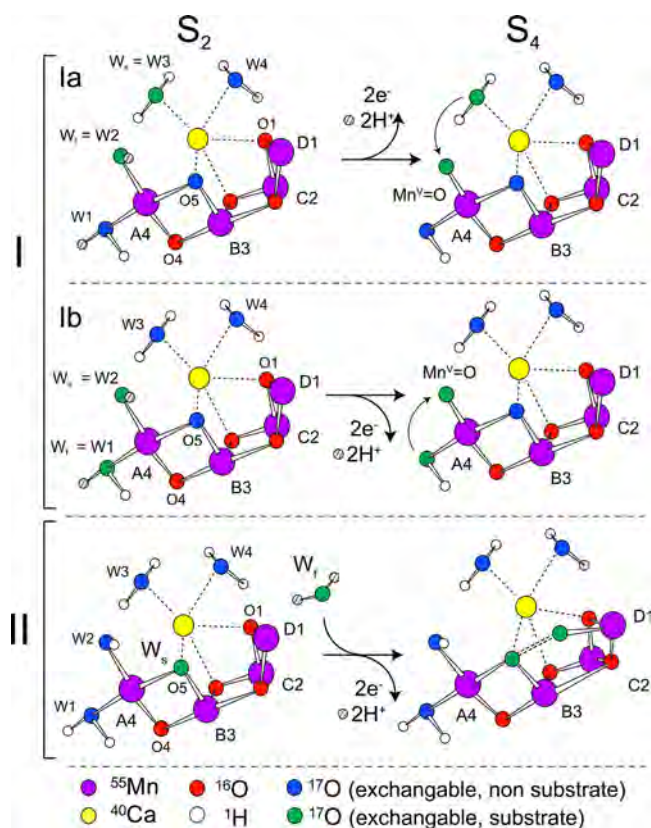
Figure 11. Possible catalytic pathways of O—O bond formation consistent with the recent crystal structure of Umena et al.[1] and the substrate exchange data presented here. Both class I (nucleophilic attack) and class II (oxo/oxyl radical coupling) are shown. The left-hand side structure represents the S_2 state probed by EPR/EDNMR. The right-hand side structure represents the inferred S_4 structure prior to O—O bond formation and release. The $Mn_{A4}(V){=}O$ may equally be considered a $Mn(IV){\equiv}O^+$ or $Mn(IV)—O^\bullet$ species.

mechanism has the advantage that it has been previously observed in Mn model systems that perform O—O bond formation. However, these systems display turnover rates orders of magnitude slower than that of the OEC.[98,99] In contrast, the radical coupling mechanism has no precedence in Mn model chemistry but is often the energetically favorable pathway for efficient O—O bond formation in second row transition-metal catalysts such as the ruthenium blue dimer (for a recent review, see ref 100). Within these considerations, a number of pathways for O—O bond formation have been proposed in the literature[6,14,15,23,48,72,101−105] (for a more complete discussion on mechanisms proposed for the OEC see refs 8, 10, 11, 48, 97, and the citations therein).

There are a number of class I type nucleophilic attack mechanisms proposed in the literature that differ in the locations of the substrate oxygen atoms within the Kok cycle and thus where O−O bond formation occurs. Here, we limit our discussion of reaction mechanisms to those broadly consistent with current crystallographic data. Specifically the two substrates are thought to be the following:

(Ia) A Ca^{2+}-bound water/hydroxo and a Mn^{IV}-oxyl or Mn^{V}-oxyl species, presumably W3 and W2.[23,102,105] In some proposals, the Ca^{2+}-bound water/hydroxo is considered to be the slow-exchanging substrate.[102]

(Ib) Two terminal water/hydroxo ligands (W1 and W2) on Mn_{A4}.[14]

(Ic) A μ-oxo/hydroxo bridge between Mn_{C2} and Mn_{D1} (O1) and the Ca^{2+}-bound W4.[101,106] The Mn μ-oxo/hydroxo is considered to be the slow-exchanging substrate.

(Id) O5 (which is a water molecule in S_1) and an as yet unidentified water.[103]

Suggestion Id is unique in that it assumes a low-oxidation state model for the OEC Kok cycle ($S_1 = Mn_4$(II, III, III, IV)), in contrast to the other models, which favor the high-oxidation state model ($S_1 = Mn_4$(III, III, IV, IV)).[103]

There is also a number of class II type radical coupling mechanisms in the literature, for reviews see refs 8, 10, 11, 48, 72, and 97. Here, we limit our discussion to the most detailed and rigorous proposal at present, which is the mechanism proposed by Siegbahn.[6] In his catalytic cycle, the slow-exchanging substrate is considered to be the O5 μ-oxo bridge between Mn_{A4} and Mn_{B3}. The exchanging fast substrate binds then at the open coordination site on the Mn_{D1} as water/hydroxo in S_2/S_3, forming an oxyl radical in S_4 (see Figure 11).[6] As detailed above, the ^{17}O-EDNMR data presented here suggests that one of the exchangeable substrate oxygen atoms in S_1 (and S_2) is a μ-oxo bridge, most likely O5 (see Figure 11). The location and protonation state (in the S_1 state) for this putative substrate position is only consistent with the class II mechanism of Siegbahn. However, the nucleophilic attack mechanisms Ia and Ib can potentially be modified to include this requirement. In the modified Ia′ (equally Ic′) type reaction, the two oxygens that form the O−O bound would be instead the Ca^{2+}-bound water/hydroxo (W3) and bridging μ-oxo (O5).[104] Similarly, in a modified Ib′ type reaction, the two Mn_{A4} oxygens that form the O−O bound would be a terminal water/hydroxo (W2) and bridging μ-oxo (O5).[104] In contrast, mechanism Id cannot be readily modified as it requires O5 to be a water ligand in S_1/S_2, which is inconsistent with ^1H/^2H-ENDOR data shown above.

For a definitive assignment of the exchangeable μ-oxo bridge observed here by ^{17}O-EDNMR data to the slowly exchanging substrate W_S, a matching of the exchange rates needs to be demonstrated. Since sufficient time resolution has not currently been achieved for the EDNMR experiments, our present data do not yet definitively assign this μ-oxo as a substrate. As such, mechanisms Ia and Ib as currently proposed are still potential pathways for catalytic O−O bond formation but not Ic as it requires an exchangeable O1 that is inconsistent with the ^{17}O-EDNMR data shown above. However, it should be noted that class I type nucleophilic attack mechanisms have been historically favored as they do not involve μ-oxo bridges, which were previously considered to be slow exchanging and thus catalytically irrelevant. As this is not the case, a concerted tetramer mechanism, such as that proposed by Siegbahn,[6] which uses the unique geometry of the Mn_4O_5Ca cluster to bind and position the two substrates, presents a more appealing pathway than that of momomeric Mn chemistry.

5. CONCLUSIONS

In this article, the nature of the substrate bound to the OEC poised in the S_1 state has been addressed. It is shown that one of the five μ-oxo bridges and at least one of the two terminal water ligands of Mn_{A4}, identified in the recent X-ray structure of Umena et al.,[1] contribute to the measured ^{17}O-EDNMR signal as seen using W-band EPR spectroscopy. Furthermore, it is shown that all "waters" exchange within 15 s, consistent with substrate exchange as assessed using time-resolved mass spectrometry. The identity of the exchangeable μ-oxo bridge was resolved using model complex data. In these models, it is shown that the μ-oxo bridge motif is well characterized by the hyperfine tensor anisotropy. The hyperfine tensor anisotropy and orientation observed for the exchangeable μ-oxo bridge of the OEC constrain its position to either O4 or O5, that is, the μ-oxo bridges that connects the outer Mn to the Mn_3O_3Ca open-cuboidal unit.

The observation that a μ-oxo bridge can exchange on time scales similar to that of the substrate and that the bridge is fully deprotonated in S_2 both support the mechanism of O−O bond formation put forward by Siegbahn.[6] Here, the reaction pathway proceeds via an oxo/oxyl coupling mechanism in S_4. Interestingly, this model for water oxidation excludes the binding of both substrates in the resting states (S_0, S_1) of the catalyst. This feature may in part explain the high selectivity of the OEC toward O_2 formation disfavoring "catalase like" two-electron chemistry. While the structural change that would allow a second substrate (W_f) to bind at the open coordination site of the Mn_{D1} remains unclear, a growing body of evidence from both EPR and FTIR studies suggests that binding is associated with S_3 formation.

■ ASSOCIATED CONTENT

Ⓢ Supporting Information

Additional details for ^1H hyperfine coupling data for the S-states (OEC); literature ^{17}O hyperfine/quadrupole couplings for metallocofactors/model complexes; spin Hamiltonian formalism for the Mn model system; spin Hamiltonian formalism of the Mn tetramer system; control ESE detected field sweep W- and Q-band EPR of the OEC; EDNMR/ENDOR data processing; spin Hamiltonian simulations of the ^{17}O EDNMR spectra; W-band ^{17}O-ENDOR of $^{14}N(^{15}N)$-PSII; material describing the multipole coupling model; ^1H/^{17}O multipole coupling estimates for all O/H within 5 Å of the OEC (Umena et al.[1]); simulations of ^1H/^{17}O-ENDOR data; ^{17}O hyperfine tensor orientations for all coordinating oxygen ligands of the OEC.; simulation details regarding the spin Hamiltonian simulations in Figure 9; additional simulations of the ^{17}O-EDNMR profile using the structural constraints in the Supporting Information, S10−S12; theoretical EPR parameter calculations from BS-DFT; and references. This material is available free of charge via the Internet at http://pubs.acs.org.

■ AUTHOR INFORMATION

Corresponding Author
nicholas.cox@cec.mpg.de; wolfgang.lubitz@cec.mpg.de

Notes
The authors declare no competing financial interest.

REFERENCES

(1) Umena, Y.; Kawakami, K.; Shen, J.-R.; Kamiya, N. *Nature* **2011**, *473*, 55−60.

(2) Ferreira, K. N.; Iverson, T. M.; Maghlaoui, K.; Barber, J.; Iwata, S. *Science* **2004**, *303*, 1831−1838.

(3) Loll, B.; Kern, J.; Saenger, W.; Zouni, A.; Biesiadka, J. *Nature* **2005**, *438*, 1040−1044.

(4) Yano, J.; Kern, J.; Sauer, K.; Latimer, M. J.; Pushkar, Y.; Biesiadka, J.; Loll, B.; Saenger, W.; Messinger, J.; Zouni, A.; Yachandra, V. K. *Science* **2006**, *314*, 821−825.

(5) Lubitz, W.; Reijerse, E. J.; Messinger, J. *Energy Environ. Sci.* **2008**, *1*, 15−31.

(6) Siegbahn, P. E. M. *Acc. Chem. Res.* **2009**, *42*, 1871−1880.

(7) Dau, H.; Zaharieva, I. *Acc. Chem. Res.* **2009**, *42*, 1861−1870.

(8) McEvoy, J. P.; Brudvig, G. W. *Chem. Rev.* **2006**, *106*, 4455−4483.

(9) Tommos, C.; Babcock, G. T. *Acc. Chem. Res.* **1998**, *31*, 18−25.

(10) Hillier, W.; Messinger, J. *Mechanism of Photosynthetic Oxygen Production*; Springer: The Netherlands, 2005; Vol. *1*.

(11) Messinger, J.; Noguchi, T.; Yano, J. In *Molecular Solar Fuels*; Wydrzynski, T., Hillier, W., Eds.; Royal Society of Chemistry Publishing: Cambridge, U.K., 2012, 163−207.

(12) Kok, B.; Forbush, B.; McGloin, M. *Photochem. Photobiol.* **1970**, *11*, 457−467.

(13) Yano, J.; Yachandra, V. K. *Inorg. Chem.* **2008**, *47*, 1711−1726.

(14) Kusunoki, M. *Biochim. Biophys. Acta* **2007**, *1767*, 484−492.

(15) Dau, H.; Grundmeier, A.; Loja, P.; Haumann, M. *Philos. Trans. R. Soc., B* **2008**, *363*, 1237−1244.

(16) Yano, J.; Kern, J.; Irrgang, K.-D.; Latimer, M. J.; Bergmann, U.; Glatzel, P.; Pushkar, Y.; Biesiadka, J.; Loll, B.; Sauer, K.; Messinger, J.; Zouni, A.; Yachandra, V. K. *Proc. Natl. Acad. Sci. U.S.A.* **2005**, *102*, 12047−12052.

(17) Messinger, J.; Seaton, G.; Wydrzynski, T.; Wacker, U.; Renger, G. *Biochemistry* **1997**, *36*, 6862−6873.

(18) Pushkar, Y. L.; Yano, J.; Sauer, K.; Boussac, A.; Yachandra, V. K. *Proc. Natl. Acad. Sci. U.S.A.* **2008**, *105*, 1879−1884.

(19) Ames, W.; Pantazis, D. A.; Krewald, V.; Cox, N.; Lubitz, W.; Neese, F. *J. Am. Chem. Soc.* **2011**, *133*, 19743−19757.

(20) Cox, N.; Rapatskiy, L.; Su, J.-H.; Pantazis, D. A.; Sugiura, M.; Kulik, L.; Dorlet, P.; Rutherford, A. W.; Neese, F.; Boussac, A.; Lubitz, W.; Messinger, J. *J. Am. Chem. Soc.* **2011**, *133*, 3635−3648.

(21) Hendry, G.; Wydrzynski, T. *Biochemistry* **2003**, *42*, 6209−6217.

(22) Hillier, W.; Wydrzynski, T. *Coord. Chem. Rev.* **2008**, *252*, 306−317.

(23) Messinger, J.; Badger, M.; Wydrzynski, T. *Proc. Natl. Acad. Sci. U.S.A.* **1995**, *92*, 3209−3213.

(24) Hillier, W.; Messinger, J.; Wydrzynski, T. *Biochemistry* **1998**, *37*, 16908−16914.

(25) Noguchi, T. *Philos. Trans. R. Soc., B* **2008**, *363*, 1189−1195.

(26) Noguchi, T.; Sugiura, M. *Biochemistry* **2002**, *41*, 15706−15712.

(27) Siegbahn, Per E. M. *Chem.—Eur. J.* **2008**, *14*, 8290−8302.

(28) Kawamori, A.; Inui, T.; Ono, T.; Inoue, Y. *FEBS Lett.* **1989**, *254*, 219−224.

(29) Aznar, C. P.; Britt, R. D. *Philos. Trans. R. Soc., B* **2002**, *357*, 1359−1366.

(30) Britt, R. D.; Campbell, K. A.; Peloquin, J. M.; Gilchrist, M. L.; Aznar, C. P.; Dicus, M. M.; Robblee, J.; Messinger, J. *Biochim. Biophys. Acta* **2004**, *1655*, 158−171.

(31) Fiege, R.; Zweygart, W.; Bittl, R.; Adir, N.; Renger, G.; Lubitz, W. *Photosynth. Res.* **1996**, *48*, 227−237.

(32) Åhrling, K. A.; Evans, M. C. W.; Nugent, J. H. A.; Ball, R. J.; Pace, R. J. *Biochemistry* **2006**, *45*, 7069−7082.

(33) Martínez, J. I.; Yruela, I.; Picorel, R.; Alonso, P. J. *J. Phys. Chem. B* **2010**, *114*, 15345−15353.

(34) Thomann, H.; Bernardo, M.; Goldfarb, D.; Kroneck, P. M. H.; Ullrich, V. *J. Am. Chem. Soc.* **1995**, *117*, 8243−8251.

(35) Burdi, D.; Willems, J.-P.; Riggs-Gelasco, P.; Antholine, W. E.; Stubbe, J.; Hoffman, B. M. *J. Am. Chem. Soc.* **1998**, *120*, 12910−12919.

(36) Carepo, M.; Tierney, D. L.; Brondino, C. D.; Yang, T. C.; aPamplona, A.; Telser, J.; Moura, I.; Moura, J. J. G.; Hoffman, B. M. *J. Am. Chem. Soc.* **2001**, *124*, 281−286.

(37) Astashkin, A. V.; Feng; Raitsimring, A. M.; Enemark, J. H. *J. Am. Chem. Soc.* **2004**, *127*, 502−503.

(38) Enemark, J. H.; Raitsimring, A. M.; Astashkin, A. V.; Klein, E. L. *Faraday Discuss.* **2011**, *148*, 249−267.

(39) Baute, D.; Goldfarb, D. *J. Phys. Chem. A* **2005**, *109*, 7865−7871.

(40) Hansson, Ö.; Andréasson, L.-E.; Vänngård, T. *FEBS Lett.* **1986**, *195*, 151−154.

(41) Turconi, S.; MacLachlan, D. J.; Bratt, P. J.; Nugent, J. H. A.; Evans, M. C. W. *Biochemistry* **1997**, *36*, 879−885.

(42) Evans, M. C. W.; Nugent, J. H. A.; Ball, R. J.; Muhiuddin, I.; Pace, R. J. *Biochemistry* **2004**, *43*, 989−994.

(43) Su, J.-H.; Lubitz, W.; Messinger, J. *J. Am. Chem. Soc.* **2007**, *130*, 786−787.

(44) Su, J.-H.; Lubitz, W.; Messinger, J. *J. Am. Chem. Soc.* **2011**, *133*, 12317−12317.

(45) García-Rubio, I.; Martínez, J. I.; Picorel, R.; Yruela, I.; Alonso, P. J. *J. Am. Chem. Soc.* **2003**, *125*, 15846−15854.

(46) McConnell, I. L.; Grigoryants, V. M.; Scholes, C. P.; Myers, W. K.; Chen, P. P. Y.; Whittaker, J. W.; Brudvig, G. W. *J. Am. Chem. Soc.* **2012**, *134*, 1504−1512.

(47) Usov, O. M.; Grigoryants, V. M.; Tagore, R.; Brudvig, G. W.; Scholes, C. P. *J. Am. Chem. Soc.* **2007**, *129*, 11886−11887.

(48) Messinger, J. *Phys. Chem. Chem. Phys.* **2004**, *6*, 4764−4771.

(49) Tagore, R.; Crabtree, R. H.; Brudvig, G. W. *Inorg. Chem.* **2007**, *46*, 2193−2203.

(50) Schosseler, P.; Wacker, T.; Schweiger, A. *Chem. Phys. Lett.* **1994**, *224*, 319−324.

(51) Vinck, E.; Van Doorslaer, S.; Dewilde, S.; Mitrikas, G.; Schweiger, A.; Moens, L. *J. Biol. Inorg. Chem.* **2006**, *11*, 467−475.

(52) Florent, M.; Kaminker, I.; Nagarajan, V.; Goldfarb, D. *J. Magn. Reson.* **2011**, *210*, 192−199.

(53) Klein, E. L.; Raitsimring, A. M.; Astashkin, A. V.; Rajapakshe, A.; Johnson-Winters, K.; Arnold, A. R.; Potapov, A.; Goldfarb, D.; Enemark, J. H. *Inorg. Chem.* **2012**, *51*, 1408−1418.

(54) Kaminker, I.; Goldberg, H.; Neumann, R.; Goldfarb, D. *Chem.—Eur. J.* **2010**, *16*, 10014−10020.

(55) Sugiura, M.; Boussac, A.; Noguchi, T.; Rappaport, F. *Biochim. Biophys. Acta* **2008**, *1777*, 331−342.

(56) Boussac, A.; Rappaport, F.; Carrier, P.; Verbavatz, J. M.; Gobin, R.; Kirilovsky, D.; Rutherford, A. W.; Sugiura, M. *J. Biol. Chem.* **2004**, *279*, 22809−22819.

(57) Ishida, N.; Sugiura, M.; Rappaport, F.; Lai, T. L.; Rutherford, A. W.; Boussac, A. *J. Biol. Chem.* **2008**, *283*, 13330−13340.

(58) Sander, J.; Nowaczyk, M.; Buchta, J.; Dau, H.; Vass, I.; Deák, Z.; Dorogi, M.; Iwai, M.; Rögner, M. *J. Biol. Chem.* **2010**, *285*, 29851−29856.

(59) Nowaczyk, M. M.; Krause, K.; Mieseler, M.; Sczibilanski, A.; Ikeuchi, M.; Rögner, M. *Biochim. Biophys. Acta* **2011**, *1817*, 1339−1345.

(60) Reijerse, E.; Lendzian, F.; Isaacson, R.; Lubitz, W. *J. Magn. Reson.* **2012**, *214*, 237−243.

16633

dx.doi.org/10.1021/ja3053267 | *J. Am. Chem. Soc.* 2012, 134, 16619−16634

(61) Stoll, S.; Schweiger, A. *J. Magn. Reson.* **2006**, *178*, 42–55.

(62) Schweiger, A.; Jeschke, G. *Principles of Pulse Electron Paramagnetic Resonance*; Oxford University Press: Oxford, U.K., 2001.

(63) Schäfer, K. O.; Bittl, R.; Zweygart, W.; Lendzian, F.; Haselhorst, G.; Weyhermüller, T.; Wieghardt, K.; Lubitz, W. *J. Am. Chem. Soc.* **1998**, *120*, 13104–13120.

(64) Cooper, S. R.; Dismukes, G. C.; Klein, M. P.; Calvin, M. *J. Am. Chem. Soc.* **1978**, *100*, 7248–7252.

(65) Dismukes, G. C.; Siderer, Y. *Proc. Natl. Acad. Sci. U.S.A.* **1981**, *78*, 274–278.

(66) Åhrling, K. A.; Peterson, S.; Styring, S. *Biochemistry* **1997**, *36*, 13148–13152.

(67) Messinger, J.; Robblee, J. H.; Yu, W. O.; Sauer, K.; Yachandra, V. K.; Klein, M. P. *J. Am. Chem. Soc.* **1997**, *119*, 11349–11350.

(68) Peloquin, J. M.; Campbell, K. A.; Randall, D. W.; Evanchik, M. A.; Pecoraro, V. L.; Armstrong, W. H.; Britt, R. D. *J. Am. Chem. Soc.* **2000**, *122*, 10926–10942.

(69) Randall, D. W.; Chan, M. K.; Armstrong, W. H.; Britt, R. D. *Mol. Phys.* **1998**, *95*, 1283–1294.

(70) Randall, D. W.; Sturgeon, B. E.; Ball, J. A.; Lorigan, G. A.; Chan, M. K.; Klein, M. P.; Armstrong, W. H.; Britt, R. D. *J. Am. Chem. Soc.* **1995**, *117*, 11780–11789.

(71) Kulik, L. V.; Epel, B.; Lubitz, W.; Messinger, J. *J. Am. Chem. Soc.* **2005**, *127*, 2392–2393.

(72) Kulik, L. V.; Epel, B.; Lubitz, W.; Messinger, J. *J. Am. Chem. Soc.* **2007**, *129*, 13421–13435.

(73) Britt, R. D.; Zimmermann, J. L.; Sauer, K.; Klein, M. P. *J. Am. Chem. Soc.* **1989**, *111*, 3522–3532.

(74) Stich, T. A.; Yeagle, G. J.; Service, R. J.; Debus, R. J.; Britt, R. D. *Biochemistry* **2011**, *50*, 7390–7404.

(75) Yeagle, G. J.; Gilchrist, M. L.; Walker, L. M.; Debus, R. J.; Britt, R. D. *Philos. Trans. R. Soc., B* **2008**, *363*, 1157–1166.

(76) Stull, J. A.; Stich, T. A.; Service, R. J.; Debus, R. J.; Mandal, S. K.; Armstrong, W. H.; Britt, R. D. *J. Am. Chem. Soc.* **2009**, *132*, 446–447.

(77) Plaksin, P. M.; Stoufer, R. C.; Mathew, M.; Palenik, G. J. *J. Am. Chem. Soc.* **1972**, *94*, 2121–2122.

(78) Cooper, S. R.; Calvin, M. *J. Am. Chem. Soc.* **1977**, *99*, 6623–6630.

(79) Jensen, A. F.; Su, Z.; Hansen, N. K.; Larsen, F. K. *Inorg. Chem.* **1995**, *34*, 4244–4252.

(80) Debus, R. J.; Campbell, K. A.; Gregor, W.; Li, Z.-L.; Burnap, R. L.; Britt, R. D. *Biochemistry* **2001**, *40*, 3690–3699.

(81) Teutloff, C.; Kessen, S.; Kern, J.; Zouni, A.; Bittl, R. *FEBS Lett.* **2006**, *580*, 3605–3609.

(82) Pantazis, D. A.; Orio, M.; Petrenko, T.; Zein, S.; Lubitz, W.; Messinger, J.; Neese, F. *Phys. Chem. Chem. Phys.* **2009**, *11*, 6788–6798.

(83) Beck, W. F.; De Paula, J. C.; Brudvig, G. W. *J. Am. Chem. Soc.* **1986**, *108*, 4018–4022.

(84) Boussac, A.; Sugiura, M.; Inoue, Y.; Rutherford, A. W. *Biochemistry* **2000**, *39*, 13788–13799.

(85) Boussac, A.; Rutherford, A. W.; Styring, S. *Biochemistry* **1990**, *29*, 24–32.

(86) Stich, T. A.; Whittaker, J. W.; Britt, R. D. *J. Phys. Chem. B* **2010**, *114*, 14178–14188.

(87) Raitsimring, A. M.; Astashkin, A. V.; Baute, D.; Goldfarb, D.; Caravan, P. *J. Phys. Chem. A* **2004**, *108*, 7318–7323.

(88) Schäfer, K. O. Doctoral Thesis, Technische Universität, 2002.

(89) Sage, J. T.; Xia, Y. M.; Debrunner, P. G.; Keough, D. T.; De Jersey, J.; Zerner, B. *J. Am. Chem. Soc.* **1989**, *111*, 7239–7247.

(90) Bencini, A.; Gatteschi, D. *EPR of Exchange Coupled Systems*; Springer-Verlag: Berlin, Germany, 1990.

(91) Force, D. A.; Randall, D. W.; Lorigan, G. A.; Clemens, K. L.; Britt, R. D. *J. Am. Chem. Soc.* **1998**, *120*, 13321–13333.

(92) Schinzel, S.; Schraut, J.; Arbuznikov, A.; Siegbahn, P.; Kaupp, M. *Chem.—Eur. J.* **2010**, *16*, 10424–10438.

(93) Chu, H.-A.; Sackett, H.; Babcock, G. T. *Biochemistry* **2000**, *39*, 14371–14376.

(94) Kimura, Y.; Ishii, A.; Yamanari, T.; Ono, T.-a. *Biochemistry* **2005**, *44*, 7613–7622.

(95) Hou, L.-H.; Wu, C.-M.; Huang, H.-H.; Chu, H.-A. *Biochemistry* **2011**, *50*, 9248–9254.

(96) Lohmiller, T.; Cox, N.; Su, J.-H.; Messinger, J.; Lubitz, W. *J. Biol. Chem.* **2012**, *287*, 24721–24733.

(97) Messinger, J.; Renger, G. In *Primary Processes of Photosynthesis - Part 2: Basic Principles and Apparatus*; Renger, G., Ed.; Royal Society of Chemistry Publishing: Cambridge, U.K., 2008; pp 291–349.

(98) Gao, Y.; Åkermark, T.; Liu, J.; Sun, L.; Åkermark, B. *J. Am. Chem. Soc.* **2009**, *131*, 8726–8727.

(99) Privalov, T.; Sun, L.; Åkermark, B.; Liu, J.; Gao, Y.; Wang, M. *Inorg. Chem.* **2007**, *46*, 7075–7086.

(100) Liu, F.; Concepcion, J. J.; Jurss, J. W.; Cardolaccia, T.; Templeton, J. L.; Meyer, T. J. *Inorg. Chem.* **2008**, *47*, 1727–1752.

(101) Dau, H.; Haumann, M. *Biochim. Biophys. Acta* **2007**, *1767*, 472–483.

(102) Sproviero, E. M.; Gascon, J. A.; McEvoy, J. P.; Brudvig, G. W.; Batista, V. S. *J. Am. Chem. Soc.* **2008**, *130*, 3428–3442.

(103) Jaszewski, A. R.; Petrie, S.; Pace, R. J.; Stranger, R. *Chem.—Eur. J.* **2011**, *17*, 5699–5713.

(104) Yamanaka, S.; Isobe, H.; Kanda, K.; Saito, T.; Umena, Y.; Kawakami, K.; Shen, J. R.; Kamiya, N.; Okumura, M.; Nakamura, H.; Yamaguchi, K. *Chem. Phys. Lett.* **2011**, *511*, 138–145.

(105) Barber, J.; Ferreira, K.; Maghlaoui, K.; Iwata, S. *Phys. Chem. Chem. Phys.* **2004**, *6*, 4737–4742.

(106) Dau, H.; Haumann, M. *Coord. Chem. Rev.* **2008**, *252*, 273–295.

(107) Hillier, W.; Wydrzynski, T. *Phys. Chem. Chem Phys* **2005**, *6*, 4882–4889.

(108) Pantazis, D. A.; Ames, W.; Cox, N.; Lubitz, W.; Neese, F. *Angew. Chem. Int. Ed.* **2012**, *51*, 9935–9940.

■ NOTE ADDED IN PROOF

We note that a new theoretical study of the OEC has recently appeared in online form.[108] This study rationalizes the two electronic forms of the S_2 state which give rise to the multiline and g = 4.1 signals in terms of the facile movement of the O5 bridge. It is proposed that the two states represent the O5 acting as either i) a linkage of the outer Mn (Mn_{A4}) to the cuboidal unit, where the O5 forms part of a bis-μ-oxo coordination between Mn_{A4} and Mn_{B3}; or ii) as a corner/vertex of the cuboidal unit, bridging Mn_{D1}, Mn_{C2} and Mn_{B3}. This flexibility of O5's coordination further supports its assignment to the exchangable μ-oxo bridge signal reported here and its role as a potential substrate water.